# Measurement of the transverse polarization of electrons emitted in free neutron decay

A. Kozela,[2] G. Ban,[4] A. Białek,[2] K. Bodek,[1] P. Gorel,[1,3,4] K. Kirch,[3,6] St. Kistryn,[1] O. Naviliat-Cuncic,[4,7] N. Severijns,[5] E. Stephan,[8] and J. Zejma[1]
(nTRV Collaboration)
[1]*Marian Smoluchowski Institute of Physics, Jagiellonian University, 30-059 Cracow, Poland*
[2]*Henryk Niewodniczański Institute of Nuclear Physics PAN, 31-342 Cracow, Poland*
[3]*Paul Scherrer Institut, 5234 Villigen, Switzerland*
[4]*LPC-Caen, ENSICAEN, Université de Caen Basse-Normandie, CNRS/IN2P3-ENSI, 14032 Caen, France*
[5]*Katholieke Universiteit Leuven, 3000 Leuven, Belgium*
[6]*Eidgenössische Technische Hochschule, 8006 Zürich, Switzerland*
[7]*NSCL and Department of Physics and Astronomy, MSU, East Lansing, Michigan 48824-1321, USA*
[8]*Institute of Physics, University of Silesia, 40-007 Katowice, Poland*
(Received 13 October 2011; revised manuscript received 7 February 2012; published 2 April 2012)

The final analysis of the experiment determining both components of the transverse polarization of electrons ($\sigma_{T_1}$, $\sigma_{T_2}$) emitted in the $\beta$ decay of polarized, free neutrons is presented. The $T$-odd, $P$-odd correlation coefficient quantifying $\sigma_{T_2}$, perpendicular to the neutron polarization and electron momentum, was found to be $R = 0.004 \pm 0.012 \pm 0.005$. This value is consistent with time-reversal invariance and significantly improves both the earlier result and limits the relative strength of the imaginary scalar couplings in the weak interaction. The value obtained for the correlation coefficient associated with $\sigma_{T_1}$, $N = 0.067 \pm 0.011 \pm 0.004$, agrees with the standard model expectation, providing an important sensitivity test of the experimental setup. The present result sets constraints on the imaginary part of scalar and tensor couplings in weak interactions. Implications for parameters of the leptoquark exchange model and the minimal supersymmetric model with $R$-parity violation are discussed.

DOI: 10.1103/PhysRevC.85.045501 PACS number(s): 24.80.+y, 23.40.Bw, 24.70.+s, 11.30.Er

## I. INTRODUCTION

In the standard model (SM) the description of free neutron decay involves only three parameters: (i) the relative strength of axial and vector couplings, $\lambda = g_A/g_V$; (ii) the first element of the quark mixing matrix, $V_{ud}$; and (iii) a time-reversal violating phase $\Phi$ [1]. The much larger number of observables which became accessible in novel experiments at new generation neutron sources allows not only to contribute to the determination of those parameters but also to address some basic problems reaching beyond the SM (see Refs. [2,3] for the review).

One of these is the incomplete knowledge of the physics of combined charge conjugation and parity symmetry (CP) violation. The SM with the Cabbibo-Kobayashi-Maskawa (CKM) mixing scheme [4] accounts for CP violation discovered in kaon [5] and $B$-meson [6,7] systems. It fails by many orders of magnitude to account for the most striking evidence of CP violation: the dominance of baryonic matter in the present universe [8,9].

Supported by firm theoretical considerations and strong experimental evidence [10], the combined CPT symmetry is regarded to be a strict symmetry of nature. With this assumption, CP violation is equivalent to time-reversal symmetry violation (TRV) and as a result is linked to microscopic reversibility and the principle of detailed balance. No compelling evidence of TRV has been observed in experiments testing this principle in different nuclear reactions [11], and the $T$-violating amplitude was found to be at most $10^{-3}$ of the dominant strong interaction amplitude.

To the most precise tests of time-reversal invariance belongs research for electric dipole moments of elementary particles, atoms, and molecules. Despite their impressive accuracy, one obtains only upper bounds ($2.9 \times 10^{-26}$, $5.9 \times 10^{-28}$, $3.1 \times 10^{-29}$ $e$ cm for neutrons [12], electrons [13], and $^{199}$Hg atoms [14], respectively) which are still orders of magnitude away from the SM predictions (e.g., $10^{-32}$–$10^{-34}$ $e$ cm for the neutron [15,16]), leaving a lot of room for new physics research.

The situation is more complicated in high-energy experiments or in systems with heavy-quark content. Also here it is possible to construct observables sensitive to TRV, but the sizable contributions of heavy quarks makes it difficult to disentangle between new physics and the SM-induced effects. This was the case in the first direct observation of TRV in the kaon system in the CPLEAR [17] and KTeV experiments [18]. The D0 collaboration only very recently reported the observation of a charge asymmetry like-sign dimuon production in proton antiproton collisions at 1.96-TeV center-of-mass energy, which contradicts the SM at 3.2 standard deviations [19].

During the early 1960s it was recognized that TRV may be tested also in various correlations accessible in nuclear or particles decays [20,21]. Many systems have been investigated in this way, including mesons [22], leptons [23], baryons, and nuclei (see Ref. [24] for a review). The measurement of the $R$ coefficient in $^8$Li decay, quantifying the correlation among the spin of the decaying nucleus, the electron momentum, and the electron spin, provides the most stringent direct limit on the imaginary part of tensor coupling constants of the weak interaction [25]. The discovery of new CP- or T-violating phenomena, especially in systems built of quarks of the first generation, with vanishingly small contributions from the CKM matrix-induced mechanism, would be an important milestone.

 

Free neutron decay plays a particular role in nuclear $\beta$-decay experiments searching for TRV. Due to its simplicity it is free from model-dependent corrections associated with nuclear and atomic structure. Further, final-state interaction effects, which can mimic T violation, are small in this case and can, in addition, be calculated with a relative precision better than 1% [26]. From a variety of correlation coefficients which may be built from vectors accessible in neutron decay, until now only two have been addressed experimentally. First was the angular correlation among the neutron spin, the electron momentum, and the neutrino momentum, referred to as the $D$ coefficient in the literature. It is sensitive to the relative strength $(g_A/g_V)$ and phase angle $(\Phi_{VA})$ between axial and vector currents in weak interactions and has been measured in several experiments [27–30]. At the current precision it provides the best limits to certain time-reversal violating parameters appearing in standard model extensions with leptoquarks exchange, associated with a nonzero value of $\sin\Phi_{VA}$.

In this paper we present the final analysis of the first measurement of another time-reversal violating correlation coefficient in neutron decay (the $R$ coefficient) and of the time-reversal conserving $N$ correlation, both associated with a correlation between the neutron spin, the electron momentum, and its polarization. Being sensitive to the real and imaginary parts of scalar and tensor couplings of the weak interaction they provide information complementary to the $D$ coefficient.

This is the final report of the nTRV experiment comprising data collected between 2004 and 2007. It supercedes our previous result, presenting the methods used in the data analysis in more detail and introducing a new $R$-evaluation approach based on a "double" -ratio method. The significant improvement in the accuracy of the determination of this correlation coefficient as compared to the result presented in Ref. [31] is a consequence of two major extensions in the analysis of the existing data: (i) the analysis of an additional event class with backscattered electrons trajectories contained within the vertical plane and (ii) improved determination of the effective analyzing powers of the applied Mott scatterers. Minor changes in the value of the $P$-even, $T$-even $N$ correlation coefficient are the result of new effective analyzing powers and the analysis of another event class which has also not been included in the previous analysis.

The outline of this paper is as follows. In Sec. II we introduce the measured observables and present the strategy of the experiment. The dedicated neutron beam line, detector setup and performance, as well as the hardware trigger are discussed in Sec. III. Section IV presents the data analysis and discussion of systematic effects and describes applied consistency checks. The results obtained and their implications on some extensions of the SM are compared with existing experimental data in Sec. V, and, finally, conclusions are given in Sec. VI.

## II. CORRELATIONS IN NEUTRON $\beta$-DECAY

The electron distribution function for an experiment, in which the decaying neutrons are oriented and electron energy, momentum $(E, \mathbf{p})$, and polarization are measured, is proportional to [20]

$$W(\langle\mathbf{J}\rangle, \hat{\boldsymbol{\sigma}}, E, \mathbf{p}) \propto 1 + b\frac{m}{E} + \frac{\mathbf{p}}{E}\cdot\left(A\frac{\langle\mathbf{J}\rangle}{J} + G\,\hat{\boldsymbol{\sigma}}\right) + \frac{\langle\mathbf{J}\rangle}{J}\cdot\left(Q\frac{\mathbf{p}}{E}\frac{\mathbf{p}\cdot\hat{\boldsymbol{\sigma}}}{E+m} + N\hat{\boldsymbol{\sigma}} + R\frac{\mathbf{p}\times\hat{\boldsymbol{\sigma}}}{E}\right), \quad (1)$$

where $m$ is the electron mass and $J$ and $\langle\mathbf{J}\rangle$ are the neutron spin and its expectation value, respectively. $\hat{\boldsymbol{\sigma}}$ is a unit vector onto which the electron spin is projected and $A$ is the $\beta$-decay asymmetry parameter. Higher-order terms in $\mathbf{p}$, $\mathbf{J}$, and $\hat{\boldsymbol{\sigma}}$ are neglected. $N$ and $R$ are the correlation coefficients associated with $\sigma_{T_1}$ and $\sigma_{T_2}$, respectively, where $\sigma_{T_2}$ is the transverse component of the electron polarization perpendicular to the decay plane spanned by the neutron spin and the electron momentum, and $\sigma_{T_1}$ is the component contained within this plane (Fig. 1). As the terms involving $G$ and $Q$ are proportional to the longitudinal component of electron polarization which was not accessible in the presented experiment, Eq. (1) reduces to

$$W(\mathbf{J}, \hat{\boldsymbol{\sigma}}, E, \mathbf{p}) \propto 1 + b\frac{m}{E} + \mathbf{P}\cdot\left(A\frac{\mathbf{p}}{E} + N\hat{\boldsymbol{\sigma}} + R\frac{\mathbf{p}\times\hat{\boldsymbol{\sigma}}}{E}\right), \quad (2)$$

where $\mathbf{P} = \langle\mathbf{J}\rangle/J$ represents the average neutron beam polarization. It has been pointed out in Ref. [24] that the Fierz interference term $(b\,m/E)$ affects most of the correlation measurements using neutron spin asymmetry to extract correlation coefficients in such a way that the measured quantity becomes

$$\tilde{X} = X/(1 + \langle b\,m/E\rangle) \quad (3)$$

with $X = a, A, B, D\ldots$ and the averaging is performed over the observed $\beta$ spectrum.

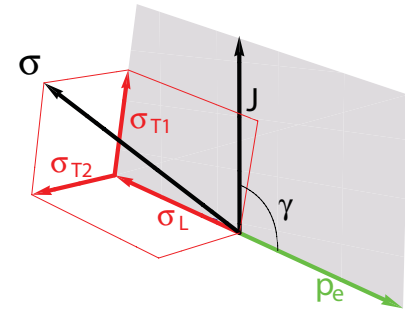


FIG. 1. (Color online) Schematic representation of neutron decay. The decay plane containing the neutron polarization $J$, the electron momentum $p_e$, and the transverse component of the electron polarization $\sigma_{T_1}$ is indicated.

### A. Final-state interaction and exotic couplings

Following Ref. [32] the general Lorenz invariant interaction Hamiltonian density of nuclear $\beta$ decay can be

written as

$$H = (\bar{p}n)[\bar{e}(C_S+C'_S\gamma_5)\nu] + (\bar{p}\gamma_\mu n)[\bar{e}\gamma_\mu(C_V+C'_V\gamma_5)\nu] + 1/2\,(\bar{p}\sigma_{\lambda\mu}n)[\bar{e}\sigma_{\lambda\mu}(C_T+C'_T\gamma_5)\nu] - (\bar{p}\gamma_\mu\gamma_5 n)[\bar{e}\gamma_\mu\gamma_5(C_A+C'_A\gamma_5)\nu] + (\bar{p}\gamma_5 n)[\bar{e}\gamma_5(C_P+C'_P\gamma_5)\nu] + \text{H.c.}, \quad (4)$$

where $C_i$ and $C'_i$ represent 10, in general complex coupling constants, which determine the symmetry properties of the weak interaction. In the minimal formulation of the SM only vector and axial-vector interactions are present ($C_V = C'_V = 1$, $C_A = C'_A = \lambda$) and all other couplings vanish ($C_i = C'_i = 0$; $i = S, T, P$). With these assumptions, both $R$ and $N$ vanish at the lowest order in neutron decay but acquire finite values when final-state interactions are included,

$$N_{\text{FSI}} \approx -\frac{m}{E}A, \quad (5)$$

$$R_{\text{FSI}} \approx -\alpha_{\text{fs}}\frac{m}{p}A, \quad (6)$$

where $\alpha_{\text{fs}}$ is the fine structure constant. For the energy distribution observed in the present experiment one obtains $N_{\text{FSI}} \approx 0.068$ and $R_{\text{FSI}} \approx 0.0006$. This means that the $R_{\text{FSI}}$ is far below the sensitivity of this experiment, while the finite value of $N$ should easily be measured.

Allowing for a small admixture of exotic couplings and keeping only terms linear in these couplings, one finds [20] that

$$N - N_{\text{FSI}} \approx -0.218\text{Re}(S) + 0.335\text{Re}(T), \quad (7)$$

$$R - R_{\text{FSI}} \approx -0.218\text{Im}(S) + 0.335\text{Im}(T), \quad (8)$$

where

$$S = (C_S + C'_S)/C_V, \quad (9)$$

$$T = (C_T + C'_T)/C_A, \quad (10)$$

are the relative strengths of scalar and tensor interactions with respect to the dominant vector and axial-vector couplings, respectively. Within these assumptions, the coefficient $b$ can be expressed as [20]

$$b \approx 0.170\text{Re}(S) + 0.830\text{Re}(T) \quad (11)$$

and would affect the measured correlations following Eq. (3). However, the additional terms are of second order in the contributions of exotic couplings and, thus, can be neglected. A nonzero value of the $R$ correlation in neutron decay would signal the existence of a nonvanishing contribution from imaginary couplings in the weak interaction, a new source of the TRV, and, as a consequence, physics beyond the SM.

The $N$ correlation depends on the real part of the same linear combination of scalar and tensor couplings as $R$. However, the discovery potential of its measurement is strongly suppressed by a significant contribution of uncertainties connected with the evaluation of the final-state interaction. There exist very few measurements of $N$ and $R$ correlations in general [22,33], and only two in nuclear $\beta$ decays [25,34].

## III. EXPERIMENT

The key feature of the nTRV experiment is the ability to measure energies and to track over relatively long distances electrons from neutron decay. This allowed for efficient use of one of the world strongest polarized, cold neutron beams as a source of electrons from neutron decay and for application of efficient electron polarimetry based on Mott backscattering [35]. An additional advantage of this principle is the unique signature of relatively rare Mott-scattering events which made them easily distinguishable off- but also on-line from an overwhelming background of electrons accompanying this, very strong, neutron beam.

Though a similar concept of electron detection has already been applied in the measurement of the neutron lifetime and the $A$ correlation coefficient [36,37], the present experimental setup outperforms the former ones, providing much more accurate reconstruction of both the electron trajectories and their energies. The experiment was performed at the SINQ facility of the Paul Scherrer Institute (Villigen, Switzerland).

### A. Cold neutron beam

A dedicated cold neutron beam line was constructed for the present experiment at channel 51 of SINQ, leading directly to the cold moderator container. The container was filled with about 20 l of liquid deuterium at 25 K. Cold neutrons from the moderator were polarized in a 1.6-m-long multichannel bender-polarizer [38] and subsequently transported to the experimental area via a rectangular channel, referred to hereafter as a condenser (Fig. 2).

Its convergent, vertical walls matched the $80 \times 150$ mm$^2$ entrance beam cross section with the about 5.5 m distant $40 \times 150$ mm$^2$ exit. The condenser's main role was to increase the neutron density at the experiment and to separate this area from a large background of fast neutrons and $\gamma$s produced in the SINQ interior and in the polarizer. To minimize background and neutron losses due to interactions with gas, the polarizer and condenser were enclosed in a vacuum chamber with 180-$\mu$m-thick and 125-$\mu$m-thick zirconium entrance and exit windows, respectively.

The application of carefully chosen, different kinds of supermirrors [39–41], with a critical reflection angle up to 3.3 times larger than that of natural nickel, applied in the polarizer and covering the walls of the beam line, allowed for

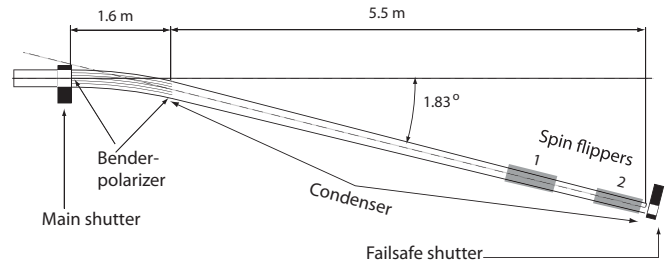


FIG. 2. Schematic top view (not to scale) of the polarized cold neutron beam line arrangement. Cold neutrons from the liquid deuterium moderator enter from the left.

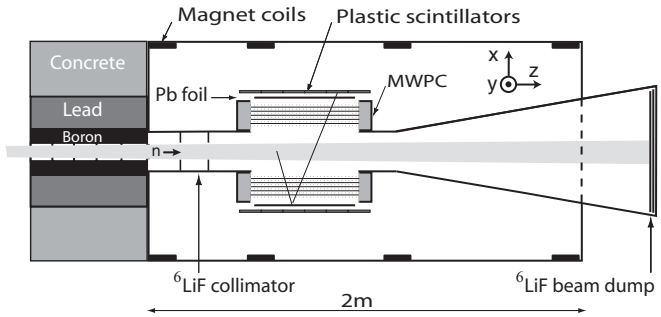


FIG. 3. Schematic top view of the experimental setup. A sample projection of an electron V-track event is shown. The coordinate system used throughout this paper is indicated.

maximum neutron polarization and transmission efficiency. A vertical spin guiding magnetic field was maintained along the beam line by a combination of permanent magnets and iron plates. The magnitude of this field was approximately constant along the polarizer and over a large part of the condenser. Two adiabatic radiofrequency (rf) spin flippers, mounted around the last section of the condenser, were used to reverse the orientation of the neutron beam polarization at regular time intervals, typically every 16 s. In order to create a field gradient, necessary for the spin-flipper operation, the magnetic field decreased monotonically from about 30 mT at the beginning of the first spin flipper to 1 mT behind the second spin flipper. Except for data collected in 2004, during the regular data taking only one spin flipper has been used—the one further away from the Mott polarimeter. This precaution was taken to decrease electromagnetic noise influencing the operation of the sensitive electronics used at the detector position.

The experimental area was shielded from the background produced in the neutron guide and polarizer by a 0.5-m-thick concrete wall with inserted boron-lead collimator (Fig. 3). The 1.3-m-long, multislit collimator defined the beam cross section to $40 \times 150$ mm$^2$ at the entrance of the Mott polarimeter. In order to minimize neutron scattering and capture, the entire beam line, from the collimator to the beam dump, was enclosed in a chamber lined with $^6$LiF polymer and filled with pure helium at atmospheric pressure.

The total flux of the collimated beam was typically about $10^{10}$ neutrons/s. The beam divergence was 0.8° in the horizontal and 1.5° in the vertical direction. A detailed study of the beam polarization at the position of the experimental setup was performed with a polarization analyzer based on the bent supermirrors concept, analogous to the one used in the polarizer. The obtained results revealed a maximum polarization of 95% in the beam center and its strong dependence on the position and on the inclination angle with respect to the beam axis. This feature hindered a reliable evaluation of the average polarization integrated over the whole beam fiducial volume. The adopted solution was to measure, in parallel to the main correlation experiment, and with the same beam and detector, also the neutron $\beta$-decay asymmetry. As the asymmetry parameter is known with high precision from other experiments, this approach allows the extraction of the average beam polarization while automatically accounting for the complicated beam phase space and the detector acceptance. The obtained results are listed in Table III.

A more detailed description of the design, operation, and performance of the cold neutron beam line can be found in Ref. [42].

### B. Detector setup and performance

The Mott polarimeter consists of two identical modules, arranged symmetrically on both sides of the neutron beam (Fig. 3). The whole structure was mounted inside a large-volume dipole magnet providing a homogeneous vertical holding field of 0.5 mT within the beam fiducial volume. Going outward from the beam, each module consists of a multiwire proportional chamber (MWPC) for electron tracking, a removable Mott scatterer (Pb foil), and a plastic scintillator hodoscope for electron energy measurement.

The main requirements which shaped the design of the MWPC were the minimal energy loss and multiple scattering of low-energy electrons and the possibly small cross section for conversion of $\gamma$ quanta into electrons, which would pose a dangerous background source. To fulfill these conditions a unique combination of special features was implemented as follows:

(i) The readout of anodes and cathodes allowed a reduction of the total thickness of the MWPC by a factor of 2.
(ii) A very light gas mixture based on helium, isobutane, and methylal (90/5/5), which, nevertheless, assured stable working conditions at anode voltages of about 1800 kV.
(iii) Thin, 25-$\mu$m Ni/Cr (80/20) wires at 5 mm and 2.5 mm pitch for anodes and cathodes, respectively,
(iv) Very thin entrance and exit windows made of 2.5-$\mu$m-aluminized Mylar foil.

Each chamber contained five planes of anodes (horizontal wires) and five planes of measuring cathodes (vertical wires), with active areas of $50 \times 50$ cm$^2$ (Fig. 4). The distance between anodes and cathodes was 4 mm and that between the consecutive anode planes was 16 mm. The average efficiency of a single plane was about 98% and 97% for anodes and cathodes, respectively.

The time measurement of individual wire hits with respect to the reference signal from the scintillator depends on the spatial density distribution of the primary ionization. Unlike in drift chambers, with electrically separated drift cells and a sense wire in their center, the adopted MWPC geometry does not allow the use of the drift time of primary ionization electrons to improve the position resolution of a single plane. However, the time information was used to improve the reconstruction of the cluster centroid for the cases in which more than two neighboring wires have responded. It was also used to check whether large clusters are not formed by two overlapping smaller clusters. This allowed for improvement of the position resolution and the double-track resolution of a single plane and was of special importance for cathodes, with an average cluster size of about 1.9 hits. The position resolution of a single plane, obtained from the

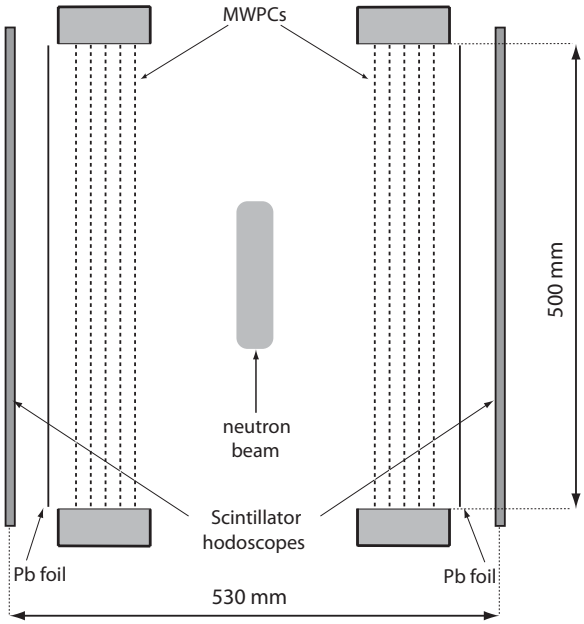


FIG. 4. Schematic front view of the experimental setup.

distribution of reconstruction residua, was about 1.2 mm and 1.7 mm rms for anodes and cathodes, respectively. Better double-track and position resolution of anodes lead to more precise and more efficient reconstruction of trajectories in the vertical coordinate, relevant for the $R$ correlation coefficient measurement.

The scintillator hodoscopes were optimized for the detection of electrons with energies up to about 1.8 MeV. This allowed the distinction of electrons originating from neutron decay from more energetic background electrons and played a crucial role in the background subtraction procedure. Each hodoscope consisted of six 1-cm-thick, 10-cm-wide, and 63-cm-long plastic scintillator slabs. Two XP3330 photomultipliers were coupled optically to both ends of the scintillator via short light guides of optimized shape. This solution allowed for reconstruction of the total electron energy with 33-keV resolution at 500 keV and 48 keV at 976 keV (see Fig. 10). The asymmetry of the light signal collected at both ends of the scintillator slab allowed the determination of the vertical ($y$) hit position with a resolution of about 6 cm, while the segmentation of the hodoscope in the horizontal direction provided a crude estimate of the $z$ coordinate. Matching the information from the precise track reconstruction in the MWPC with that from the scintillator hodoscope considerably reduced the background and random coincidences. Fast pulses from the hodoscope were also used in a trigger logic and provided the time reference signal for the MWPC wire readout.

### C. Mott scatterer

Scattering in the field of a spinless nucleus of electrons polarized in the direction perpendicular to the scattering plane reveals a left-right asymmetry due to the spin-orbit term present in the interaction potential. The purely electromagnetic

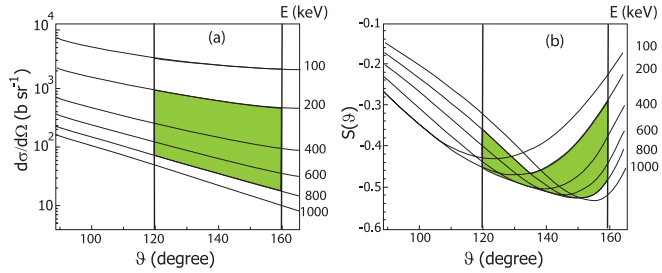


FIG. 5. (Color online) Angular distributions of the Mott-scattering cross section (a) and the Sherman function (b) for electrons of different energies on natural lead. Shaded areas show parameter regions relevant to the present experiment.

nature of this process (effects of the weak neutral currents can be safely neglected in this case) guaranties the exclusive sensitivity to the transverse polarization of the incoming electron. The resulting asymmetry is proportional to a product of the transverse polarization component of the incident electron beam and the target-specific analyzing power of the scatterer. The experiment presented here exploits particularly favorable conditions existing for electron scattering on high-$Z$ nuclei (lead) at large backward angle, where the Sherman function (analyzing power of a single nucleus [43]) reaches its highest value, and the Mott-scattering cross section is still appreciable (Fig. 5).

For a real scatterer, one has to take into account the inelastic multiple scattering with atomic electrons and, although being much less likely, plural Mott scattering at moderate angles which eventually can mimic a single Mott-backscattering event. These effects can significantly deteriorate the initial analyzing power and affect the data by their substantial dependence on the thickness of the scatterer (cf. Fig. 6) and on the incidence angle with respect to the foil surface.

In order to obtain the effective analyzing power of the scatterer, Monte Carlo simulations were performed using the GEANT4 simulation framework [44] and following the guidelines presented in Refs. [45,46]. This approach takes advantage from accurate theoretical calculations of the Sherman functions, properly accounting for atomic structure and nuclear size effects, as well as for effects due to electrons interaction

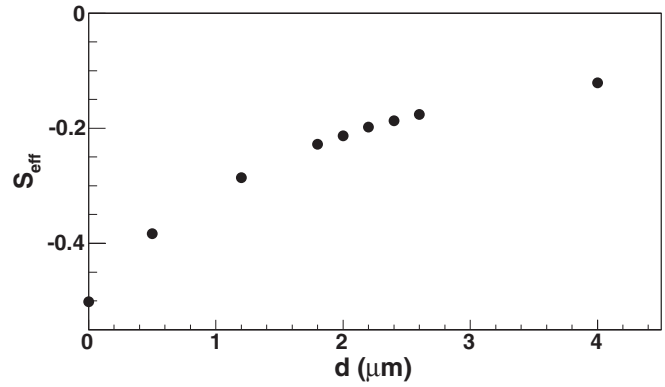


FIG. 6. Simulated effective analyzing power of lead for 400-keV electrons backscattered at an angle of 140° as a function of the lead layer thickness. Electrons incident perpendicularly to the foil.

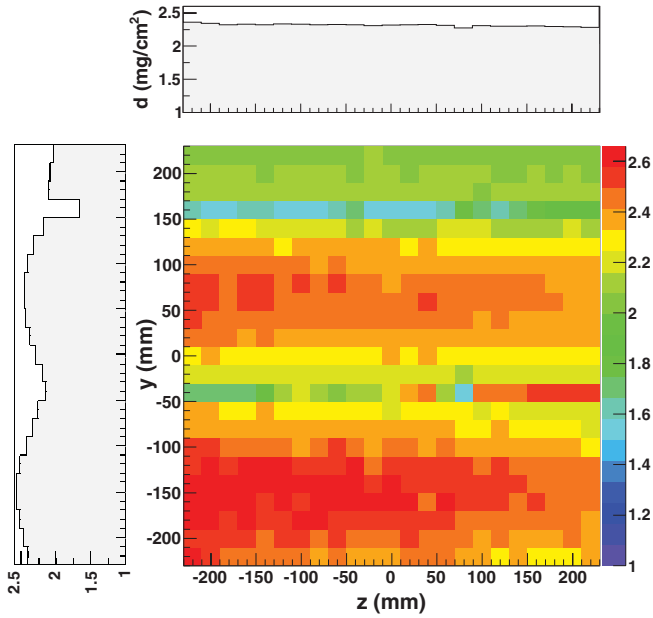


FIG. 7. (Color online) Surface density map of one Mott-target with its projection on both $y$ and $z$ axes. The deep minimum around $y = 150$ mm is due to imperfect matching of individual sheets used for the Mott-target fabrication. Smooth changes which are visible in $y$ projection are the relics of the evaporation process used for manufacturing of a single sheet.

with the medium. The accuracy of these calculations has been estimated to be better than 2% and was verified by comparison with two experimental data sets: at low (120 keV [47]) and high (14 MeV [48]) electron energies.

In the early phase of this experiment (2003–2004) a 1-$\mu$m-thick lead layer evaporated on a 2.5-$\mu$m-thick Mylar foil was used as the Mott scatterer. The bulk of the data, however, were collected in 2006 and 2007 with about twice as large surface density of the lead scatterer. Even this foil was almost transparent to the incident electrons from neutron decay, so more than 99% of them penetrated through the foil without sizable interaction with lead nuclei.

Because of very small (with respect to lead) average $Z$ of the material passed by the electron on its way between creation point and the Mott scatterer, the corresponding depolarization effects before the Mott scatterer are by a factor of almost 400 smaller and are negligible as compared to the main source of uncertainty of the analyzing power—the surface density on the foil.

Due to the Mott-foil manufacturing process, the thickness of the lead layer was not perfectly uniform. Moreover, the illumination of the foil by electrons at the experiment position was not uniform. This was included in the systematic uncertainty in the analysis presented in Ref. [31]. In order to decrease this uncertainty and to enhance the reliability of the obtained results, precise scans of the lead surface density distribution of both 2-$\mu$m Mott scatterers were performed using photon-induced characteristic radiation [49].

The resulting maps of the lead layer surface density measured with an absolute accuracy of about 55 $\mu$g/cm$^2$ (Fig. 7), together with the Monte Carlo–simulated multidimensional effective analyzing power data and the distributions of the reconstructed electron vertices on the scatterer were used to obtain the final average effective analyzing power values.

The new values are by about 7% smaller than those used in Ref. [31], with relative uncertainty reduced from 9% to about 3%.

### D. Detector electronics and hardware trigger

The entire electronics coupled directly to the detectors (sense wires of MWPC and photomultipliers) responsible for signal amplification, discrimination, and derivation of the most important early stage of the hardware trigger was designed and built especially for this experiment. The details of the implementation are described in Ref. [50], and here only the main concept of the trigger is presented.

The hardware trigger was built to collect virtually all events belonging to each of two classes:

(i) VT1-2 and VT2-1 in Fig. 8: Mott-scattered electrons with two track segments on one side and one segment accompanied by a scintillator hit on the opposite side, further referred to as "V track" (an example is shown in Fig. 3), used for the determination of the electron transverse polarization,

(ii) S1 and S2 in Fig. 8: "single-track" events with only one reconstructed track segment on the hit scintillator side, used for precise evaluation of the average beam polarization.

In order to enhance the selectivity of the trigger, two plane multiplicity signals have been constructed separately for anodes ($Y$) and cathodes ($X$) of each detector side. High plane multiplicity ($X_{iH}$, $Y_{iH}$, where $i$ indicates the side of the detector) was relevant for the detector side, which reconstructed two track segments in the MWPC, and low

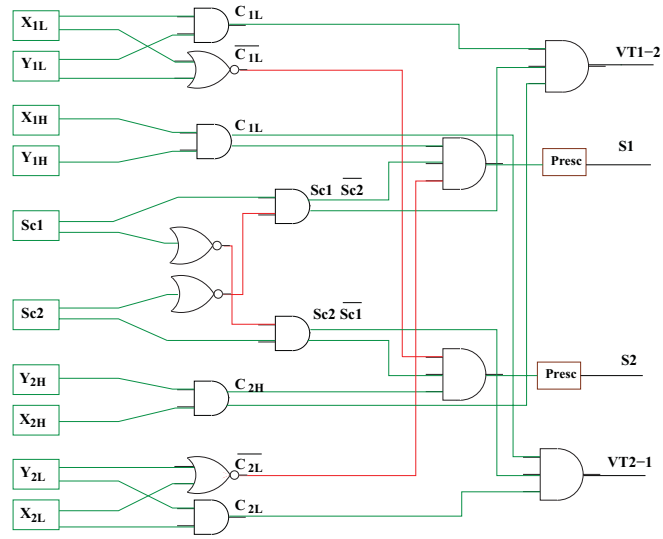


FIG. 8. (Color online) Simplified diagram of the hardware trigger. Shown is the logic of V-track (VT1-2, VT2-1) and single-track events (S1, S2) constructed from scintillator signals (Sc1/2) and chamber multiplicities low and high ($X_{1/2\,L/H}$, $Y_{1/2\,L/H}$).

multiplicity ($X_{iL}$, $Y_{iL}$) was required for the detector side with only one segment. Taking advantage of the small drift cell size and using fast OR circuits implemented on the discriminator boards of each MWPC plane, both signals were generated as early as 80 ns after the fastest scintillator pulse. This concept allowed the data acquisition to collect V-track events without losses, admitting only the most promising candidates for single-track events, with the possibility of their further reduction by the prescaler module (Fig. 8).

Typically the low (high) plane multiplicity signal was set when more than two (three) planes of the same electrode type registered at least one hit wire. With this setting the observed rates were about 800 and 8000 Hz for V track and for single-track events, respectively. In order to keep the dead time at the acceptable level below 10%, the single-track event rate was prescaled by a factor of 2.

### E. Data acquisition

For each trigger the information including pulse heights and time measurements with respect to the fastest hodoscope signal for all hodoscope hits, and time measurements for all MWPC wire hits, were digitized in fast encoding and readout- (FERA) compatible ADC (LeCroy 4300B) and TDC (LeCroy 3377) modules. In order to enhance the data throughput of the standard FERA bus, a custom CAMAC module was applied (the FERA tagger/extender). It allowed the separation of readout electronics into two logical FERA subsystems with separate gates [51]. The data from each subsystem were transferred in parallel to two pairs of VME hosted memory modules working in flip-flop mode. The memories were read out via a VME data bus controlled by a RIO2 processor running MBS data acquisition software [52] installed on the real-time operating system LynxOS. An important role of the data acquisition program was the generation of periodic interrupts, typically every second, used for read-out of monitoring scalers and for setting the spin flippers controlling the beam polarization. This software was also responsible for final logging of the data on the external mass storage and for sending a fraction of the data to the back-end computer for monitoring purposes. The average data flow rate was about 1 MB/s, which amounted to about 15% of the maximum achieved data throughput of the system.

## IV. DATA ANALYSIS

The final result of this experiment is dominated by the last and the longest data collection period. The numbers quoted in this chapter apply to this period; however, all available data were consistently analyzed in an analogous way, and the obtained results are presented and used in the calculation of the final average.

### A. Data reduction

One of the most important features of the data analysis is its hierarchical structure. The raw data collected during the experiments, coded in a compact format specific to the individual electronic modules, were first converted to "physical" format (trajectory segments, deposited energy in hit scintillators) with subsequent verification of the on-line trigger conditions. All parameters specifying these conditions were set in such a way that "good" events must not be removed regardless of their origin (i.e., from or off the beam). This allowed for the preselection of interesting event classes, thereby reducing the amount of data to be processed at the next stage of the analysis by a factor of about 12 in the case of backscattered events and by about 50% in the case of single-track events. The second step prepared the final selection of events using tighter conditions, thus, further reducing the amount of data but still allowing for some freedom in setting the most crucial parameters (listed in Sec. IV H).

TABLE I. Average electron energy losses (in keV) in most important detector layers for two electron energies and trajectories perpendicular to MWPC detection planes (along the $x$ direction).

| Material | Thickness (mm) | Energy loss (keV) for initial energy | |
|---|---|---|---|
| | | 200 | 400 |
| Helium (decay chamber) | 110 | 5.0 | 3.7 |
| MWPC Mylar window | 0.0025 | 1.9 | 1.4 |
| MWPC gas mixture | 96 | 16.8 | 12.6 |
| Mott scatterer | 0.0045 | 7.9 | 5.8 |
| Scintillator wrapping | 0.045 | 8.8 | 6.1 |

### B. Calibration of scintillator hodoscopes

The energy and position calibration of the hodoscopes was performed typically once a week using conversion electrons from a $^{207}$Bi source. A movable support driving the source (3 mm diameter of active deposit between thin titanium foils) in the $y$ and $z$ directions within the symmetry plane of the detector ($x = 0$) between the chambers was used to provide uniform illumination within the entire decay volume.

The reconstructed electron trajectories allowed the identification of the hit position along the individual scintillator and the correction for path-length-dependent electron energy losses (see Table I). As a consequence, it was possible to calibrate separately relatively short sectors of a scintillator and to obtain energy calibration specific for the position ($y$) at which the energy was deposited in the scintillator. The reconstructed deposited energy $E$ was assumed to be a linear function of the scintillator response function ($g$):

$$E = a_i(y)\ g(E_d, y) + b_i(y), \quad i = 1 \ldots 12. \tag{12}$$

The function $g$ was defined as the geometrical mean of the pulse heights recorded by the "up" and "down" photomultipliers ($c_u$, $c_d$) as follows:

$$g = \sqrt{c_u\, c_d}. \tag{13}$$

With this definition, and assuming uniform light attenuation along the scintillator, the $g$ function should be proportional to the deposited energy ($E_d$) and should not depend on $y$.

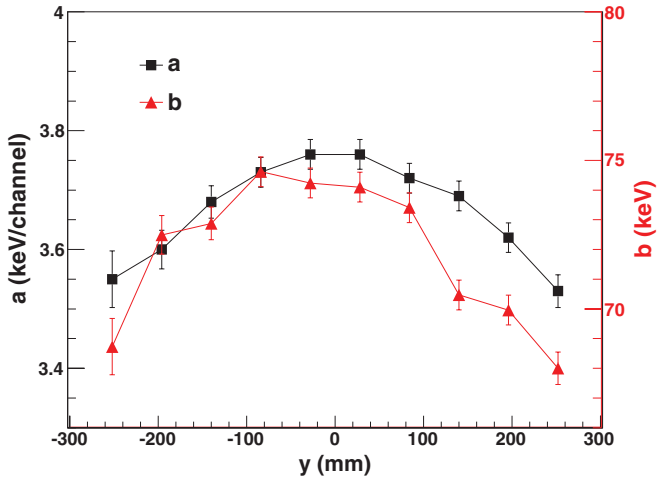


FIG. 9. (Color online) Energy calibration for one of the scintillators [see Eq. (12)]. The residual position dependence of calibration coefficients $a$ and $b$ are due to nonuniform light attenuation along the scintillator bar.

Small deviations from this assumption were compensated by the position sensitivity of the calibration coefficients $a_i$ and $b_i$ (Fig. 9).

The energy resolution can be deduced from the reconstructed $^{207}$Bi electron energy spectrum (Fig. 10). It roughly follows the primary photon statistics and amounts to 33 keV around 500 keV. The associated systematic uncertainty has been estimated to 5 keV. In order to decrease the energy spread caused by different energy losses on the way between the electron creation point (assumed to be in the symmetry plane of the detector) and the scintillator hodoscope, only events with similar path length have been selected for the calibration.

Using once again the uniform light attenuation assumption, one can show that the signal asymmetry defined as

$$r = \ln(c_u/c_d) = \frac{2\,y}{L_{\text{at}}} \tag{14}$$

should be directly proportional to $y$ and should not depend on $E_d$. Figure 11 presents the $y$ component of hit positions on

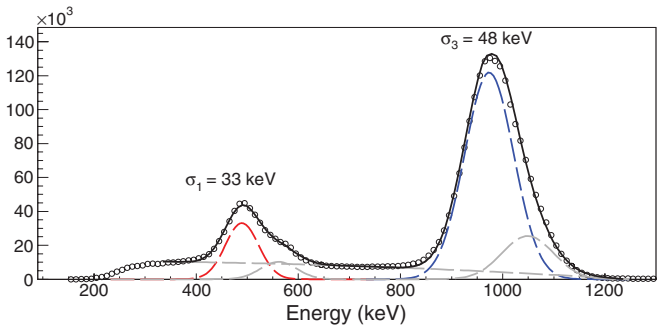


FIG. 10. (Color online) Measured $^{207}$Bi electron energy spectrum (circles) together with its decomposition into the four most important electron conversion lines (482, 558, 976, and 1052 keV) and a smooth background mainly due to electron and $\gamma$ interactions with aluminum frames of the source. The fitted widths correspond to the energy resolution of the scintillator hodoscope.

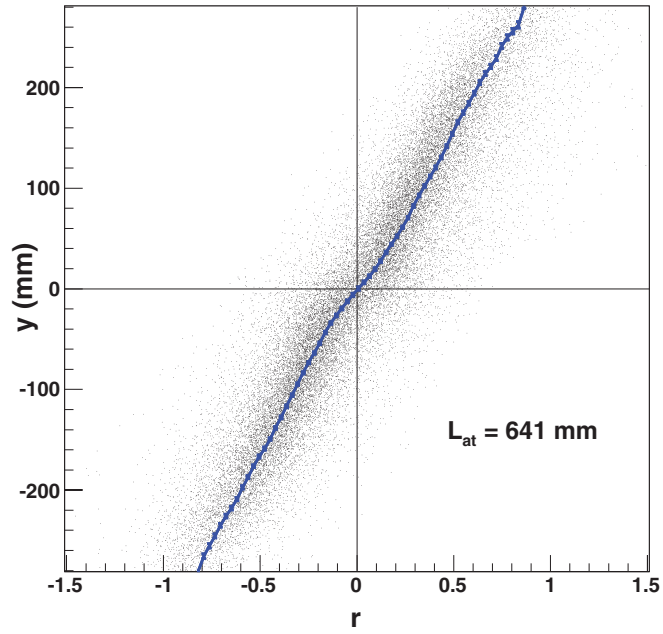


FIG. 11. (Color online) A sample position calibration $\mathcal{Y}(r)$ of one scintillator bar (solid line) superimposed on the experimental events distribution. An event is represented by the $r$ asymmetry [Eq. (14)] and hit position along the scintillator reconstructed from the MWPC information. The nonlinearity due to nonuniform light attenuation along the scintillator is clearly visible. $L_{\text{at}}$ corresponds to the average light attenuation length, Eq. (14).

the hodoscope reconstructed from the MWPC information and plotted against the $r$ asymmetry. The correlation between both observables is obvious. The large width of the band reflects the modest position resolution of the scintillator. The average $r$ at a given position $y$ was used to obtain the position calibration of an individual scintillator $\mathcal{Y}(r)$. It should be noted that this calibration was not perfectly linear, which again indicates a small departure from the uniform light attenuation assumption.

### C. Data selection and event reconstruction

The first step of the data selection procedure is a fine-tuning of the coincidence time windows in which hodoscope and MWPC hits are accepted in order to reduce event contamination with accidental coincidences. The resulting width of the time window used for the MWPC hits (180 ns) accounts for the maximum possible drift time of primary ionization electrons in the drift cell and for the time walk due to variations of the signal rise time. As the time information from scintillators was affected only by the time walk, the length of the corresponding gate for the hodoscope signals could have been much shorter and amounted to 50 ns.

For a valid hodoscope hit, the coincidence between the photomultipliers attached to both ends of one scintillator was required. In general, only one such hit was allowed in both hodoscopes. Exception was made for the cases when two neighboring scintillator slabs responded. This allowed for the selection of electrons reaching the hodoscope at the scintillators edges which deposited their energy partially in two

neighboring scintillators. Those events played an important role in the determination of the position resolution of track reconstruction at the hodoscope position, based on the position information from the anodes.

As already mentioned in Sec. III B, the information from the MWPC was reduced to the cluster centroids. The average cluster size was about 1.4 and 1.9 wires for anodes and cathodes, respectively. Clusters consisting of more than four consecutive wires were investigated in order to check whether they were formed by two overlapping clusters. The splitting condition was derived from the analysis of the time information of all hit wires belonging to this cluster and relied on the presence of two significant minima in the corresponding time distribution. As double clusters are naturally present in vertex topology (with their relative distance decreasing for wire planes closer to the Mott target), this filter was particularly important to increase the detection efficiency of V-track events. Clusters larger than 16 wires have been rejected as a possible electronics noise (16 channels were grouped in one preamplifier-discriminator card).

Straight lines were then fitted to the obtained hit patterns separately in anodes and in cathodes using a combinatoric algorithm and the minimum $\chi^2$ criterion. To be accepted, a track projection had to be detected in at least three wire planes. An event was rejected if at least one complete track segment (seen in both projections) was registered in excess of the expected number of segments, that is, exactly one segment at the hit hodoscope side, and, in the case of V-track events, additionally two segments at the opposite detector side.

In order to reduce background consisting of electrons produced in the solid parts of the detector, only track segments whose prolongations were contained within the active area of the opposite MWPC were accepted. This allowed use of the two innermost planes of the opposite chamber as a veto detector and, as a consequence, to confine significantly the volume of possible electron origins.

The reconstructed track segments were confronted with a set of conditions checking the consistency of the reconstructed event. The extension of the segment reconstructed in the MWPC at the hit hodoscope side should point, within a given tolerance, to the hit scintillator slab and should match the $y$ position reconstructed from the "up-down" asymmetry of the corresponding pulse height signals. In the case of V-track events, two lines in each projection were expected at the detector side which registered the Mott-scattering vertex. The $x$ coordinate of the vertices reconstructed in both projections should match within a tolerance given by the MWPC angular resolution. Similarly, matching in both projections was required between the segment reconstructed at the hit scintillator side and one of the two segments at the opposite side. No scintillator hit in the vicinity of the reconstructed vertex was allowed for a valid Mott-backscattering event.

Additional event classes, absent in the previous publication (Ref. [31]) and included in the analysis presented in this paper, consist of cases for which the Mott-scattering vertex was detected only in one projection ($y$-$z$ or $x$-$z$). Particularly interesting are events scattered close to or in the vertical plane. For these the projections of both segments in the $x$-$z$ plane overlap and are reconstructed as only one line. The signature of such event is weaker: since one vertex is missing, one important matching condition (vertices $x$ coordinates) drops out. Some compensation of this relaxation was achieved by increasing from three to four the threshold for the minimum plane multiplicity of the accepted line fitted in this projection. This is justified since each wire along such a double track collects twice as much charge as in the normal case. It should be noted that the $x$-$z$ projection was measured by cathodes, i.e., electrodes with significantly worse double-track resolution than anodes. This increased the number of such events, referred to as "vertical single-vertex events." This event class exhibits maximal and exclusive sensitivity to the $R$ correlation, on average 2 times higher than the primary double-vertex event class (see discussion of geometrical form factors in Sec. IV G).

The analogous event class, with one vertex reconstructed by cathode planes accompanied by only one track segment reconstructed in anodes, is much less numerous than the vertical single-vertex event class. This is due to the lower efficiency, position resolution, and double-track resolution of cathodes. Those events are sensitive almost exclusively to the $N$ correlation coefficient.

In the last step of the event reconstruction process, each event was assigned to one of several event classes determining its role in the further analysis. The most important categories were related to external conditions (the state of beam polarization and presence of the Mott target) and event geometry (from and off the beam, from and off the Mott-foil). The total numbers of reconstructed events are listed in Table II separately for all data collection periods.

### D. Effects of magnetic field

All matching conditions discussed above as well as the event geometry were affected by the magnetic field. In order to attain the required uniformity of the spin-holding field in the beam fiducial volume, the entire detector was immersed in a constant, large-volume magnetic field, produced by a magnet consisting of two soft iron plates and eight iron core coils (Fig. 3). Special care has been taken in order to shield all photomultipliers against the influence of this field. This has been achieved with a double layer of mu-metal shielding around each photomultiplier.

The effect of the magnetic field on the detected electrons is twofold. Their spins precess at the Larmor frequency and their trajectories are bent so that their $x$-$z$ projection becomes an arc. For the measurement of the transverse polarization of electrons those effects are potentially dangerous, since the polarization is produced and analyzed at distant locations (neutron decay and Mott scattering). However, since the electron $g$ factor is almost equal to 2, the spin precession almost exactly follows the momentum rotation. The maximum remnant effect, due to the "$g - 2$" factor, is well below one arc minute in this experiment and, therefore, is irrelevant for the achieved accuracy. There are, however, other consequences of the bending of the electron trajectories. Some of them can be accounted for, whereas others are discussed in order to demonstrate why they do not influence the final result.

TABLE II. Average lead surface density $d$ of the used Mott target and total numbers of reconstructed single-track events $S$, double-vertex events $VV$, and events with one vertex in anodes $V_a$ and cathodes $V_c$ for all data collection periods (in units of thousands).

| Run | $d$ ($\mu$g/cm$^2$) | $S$ (1000) | $VV$ (1000) | $V_a$ (1000) | $V_c$ (1000) |
|---|---|---|---|---|---|
| 2003 | $1.13 \pm 0.16$ | 12 000 | 19 | | |
| 2004 | $1.13 \pm 0.16$ | 43 000 | 74 | | |
| 2006 | $2.46 \pm 0.05$ | 28 000 | 312 | 106 | 28 |
| 2007 | $2.46 \pm 0.05$ | 334 000 | 1750 | 711 | 248 |
| Total | | 417 000 | 2152 | 817 | 276 |

The deviation $\rho$ of the electron trajectory from the straight line depends strongly on the distance $d$ traveled by the electron in the magnetic field. Neglecting energy losses it can be approximated as

$$\rho \approx d \tan\left[\frac{1}{2}\arcsin\left(\frac{d}{R}\right)\right], \tag{15}$$

where $R$ is the curvature radius which, for the lowest electron energy detected in this experiment, amounts to about 3 m. From this it follows that in the worst case the deviation of the real trajectory from a straight line within one MWPC is below 0.5 mm. Considering the average size of clusters in cathodes ($\approx$14 mm), such a small correction can be neglected and one may safely use a linear fit to the data. This is not the case if one considers prolongations of the obtained lines to the Mott target, to the scintillator hodoscope, or to the opposite MWPC. Then the effects can be substantial, but knowing the electron energy and the magnetic field strength they can be accounted for.

A strict correction would require taking into account continuous energy losses along the electron path. However, in view of the much larger effect of electron multiple scattering, this correction has been simplified by using the average electron energy along the considered path segment. Subsequently, the line fitted in the MWPC was treated as a tangent to the circular trajectory with a radius corresponding to this average energy. Trajectories obtained in this way were then used to calculate extrapolated electron positions and incidence angles at beam, hodoscope, Mott target, and so on.

Surprisingly, even a weak magnetic field can have a significant influence on the efficiency of V-track reconstruction. In order to understand this effect, two kinds of V tracks must be introduced. In the following they will be referred to as convex and concave (Fig. 12). For convex V tracks the distance between both trajectories measured within each wire plane (along the $z$ direction) is always larger than for its concave analog. This difference reaches its maximum around the outermost planes, closest to the Mott target, at the place where the separation of clusters belonging to both arms of the vertex reaches its minimum. This causes a difference in the probability for two clusters in the same plane to overlap and, as a consequence, increases the detection efficiency of convex V tracks and decreases this efficiency for concave V tracks. Of course, the same effect, however, with decreasing significance, occurs also in other MWPC planes. Another effect may be described as focusing (for convex) or defocusing (for concave) of the long arm of a V track on the active area of the opposite detector. It acts coherently with the previous one, further increasing (decreasing) the detection efficiency for convex (concave) V tracks.

In order to reduce the impact of all effects induced by the guiding magnetic field, its magnitude has been reduced from 1 mT, used between 2003 and 2006, to 0.45 mT in the 2007 data collection period. Nevertheless, the effects persist and can readily be observed (see, e.g., Figs. 19 and 24).

### E. Background correction

Two kinds of background have been taken into account and corrected for. The first, referred to here as the "off-beam" background, is present in single-track and in V-track event classes. It comprises all electrons not originating directly from neutron decay in the beam fiducial volume (e.g., electrons produced in nuclear decay after neutron capture, electrons from the Compton effect, large-angle scattering, accidental coincidences, etc.). The second kind, "foil-out" background, applies only to the V-track events. It accounts mainly for limited position accuracy of the vertex reconstruction.

For the "off-beam" background, the number of electrons not originating from the free neutron decay was determined by comparing energy spectra of two event classes: (i) events for which the reconstructed electron trajectory crossed the neutron beam volume ("from beam") and (ii) events for which the electron origin was outside the neutron beam ("off beam"). The procedure relies on the assumption that the spectral shape of the background is the same for both event classes, while the characteristic neutron $\beta$-decay spectrum with end-point energy of 782 keV is present only in the "from-beam" class

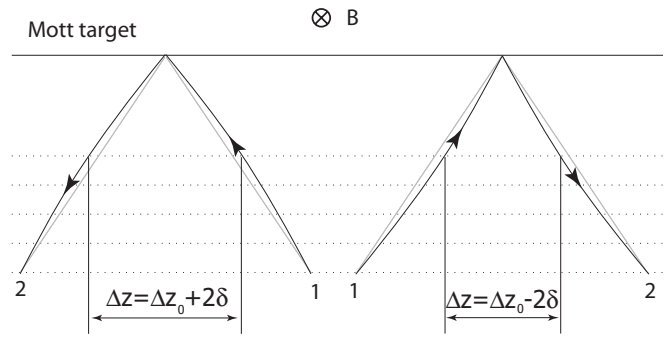


FIG. 12. Convex and concave vertices. $\delta$ corresponds to the displacement of the electron trajectory due to the magnetic field, measured along the $z$ axis at each wire plane.

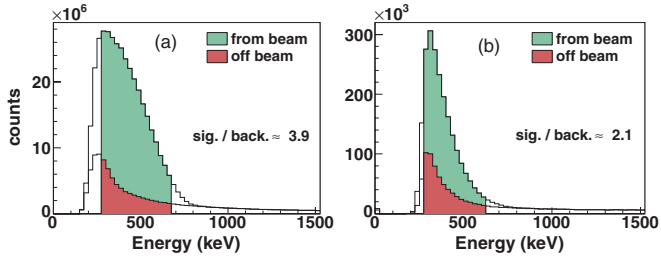


FIG. 13. (Color online) Energy distributions of signal (green) and background contributions (red) for single-track events (a) and the double-vertex event class (b). Shaded areas indicate the "signal" energy range used in the final calculations.

(Fig. 13). This allows for scaling the "off-beam" background distribution such that it matches the high-energy part of the "from-beam" energy spectrum. For this assumption to hold, the "off-beam" range has to be carefully chosen for both the inclination angle and the extrapolated origin of the tracks at the opposite detector side [35]. These conditions have to account for the angular resolution of the MWPC, the beam density distribution, and its divergence. The better signal-to-background ratio obtained for single-track events can be attributed to their much larger number what allowed for a much tighter setting of all geometrical cuts.

The validity of this background subtraction method was verified by comparing background-corrected energy spectra with the simulated $\beta$-decay spectra in which energy losses and detector resolution were taken into account.

Such a comparison is shown in Fig. 14 for single tracks and for the Mott-scattering events. In the latter case, the modification of the $\beta$ spectrum induced by the energy and angular dependence of the Mott-scattering cross section is clearly visible. Electronic thresholds are not included in the simulation—this is why the measured and simulated distributions do not match at the low-energy side. In contrast, the matching at the high-energy side is nearly perfect for single-track events (Fig. 15). Due to energy losses that are not well defined (in particular, the determination of the depth at which the Mott scattering took place within the lead scatterer is far beyond the accuracy of the electron tracking), an analogous comparison, at a similar level of accuracy, is not possible in the case of V-track events.

The lack of two important matching conditions (matching of $x$ coordinates of the vertices reconstructed in vertical and in

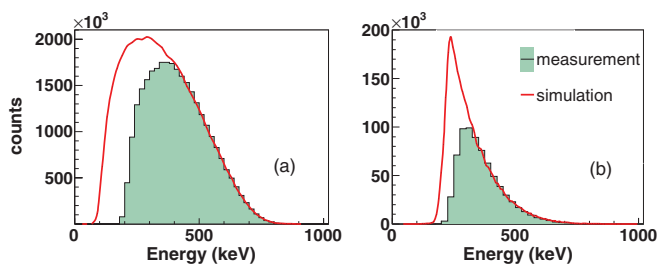


FIG. 14. (Color online) Background-corrected experimental energy distributions (shaded areas) of (a) single-track and (b) double-vertex V-track events compared with simulations.

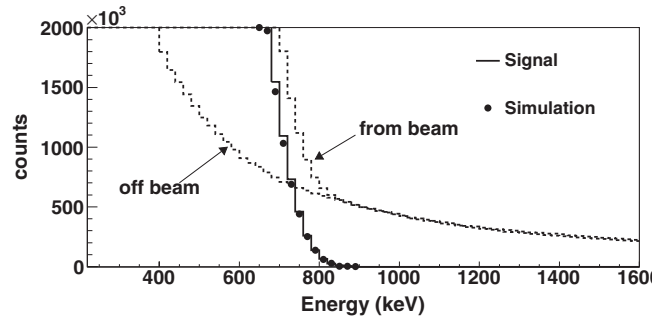


FIG. 15. Detailed view of the energy distributions of the "from-beam" and "off-beam" single-track events in the vicinity of the electron end-point energy for a defined range of electron emission angles. The agreement between the measured (solid line) and simulated signal distribution (solid circles) is near perfect.

horizontal planes and between two segments of V track's "long arm" in one projection) is the reason for the worse signal-to-background ratio observed in event classes with the single-vertex signature (Fig. 16). The difference between events with the vertex reconstructed either in cathodes or in anodes can be explained by the worse double-track resolution of cathodes and the horizontal geometry of the beam.

The same background type can be observed in the $y$ projection of the position distributions of the extrapolated origins for low- and high-energy electrons. The origin of the electron track was taken to be the intersection between its trajectory and the symmetry plane of the detector ($x = 0$). This approximation is justified by the narrow beam size along the $x$ coordinate ($\pm 2$ cm) defined by the $^6$Li beam collimator. The clear profile of the neutron beam can be recognized in the position distributions of low-energy electrons ($E < 750$ keV) in contrast to the distributions of events with higher energy (Fig. 17). The significant difference in the background distribution for double-vertex events as compared to the case of single-track events can be explained by the tighter setting of the geometrical cuts and by the dependence of the V-track detection efficiency on the Mott-scattering angle. As already discussed, for more acute vertices the probability that clusters overlap increases what, as a consequence, enhances the contribution of events with more obtuse vertices. In the end, the effect is that the distribution of the vertical coordinate of V-track origins differs slightly from that of single-track

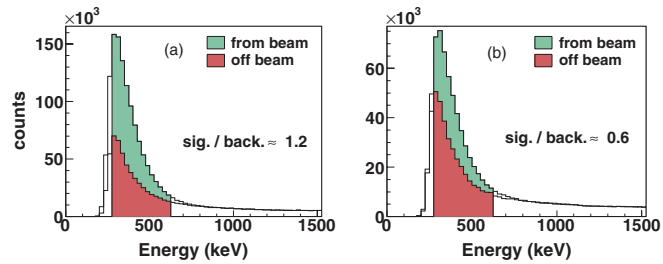


FIG. 16. (Color online) Energy distribution of signal (green) and background contributions (red) for single-vertex events in anodes and cathodes [(a) and (b), respectively]. Shaded areas indicate the "signal" energy range used in the final calculations.

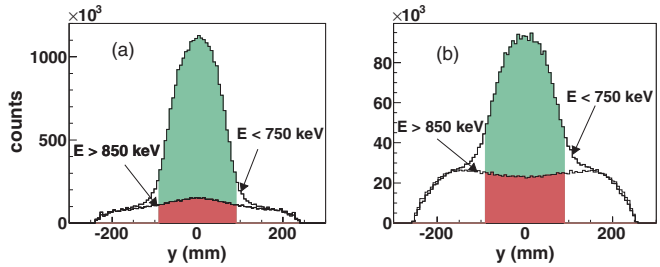


FIG. 17. (Color online) Beam profile seen in the position distribution of the extrapolated electron origins for single-track (a) and V-track events (b) for low- and high-electron energies. Shaded areas indicate the position range accepted as the "from-beam" region.

events. This means that if the beam polarization depends on $y$, then the recorded sample of V-track events acquires different average beam polarization as that deduced from the analysis of single-track events. This effect has been studied with the beam polarization dependency as measured in Ref. [42]. The resulting correction is $0.7 \times 10^{-3}$. The conclusion that this effect is negligible is also supported by the polarization analysis for the V-track event class which will be presented in the next section.

The $y$-component position distribution of V-track origins for events with only one reconstructed vertex in cathodes resembles that of single tracks but the signal-to-background ratio is much worse than for events for which only one vertex was reconstructed in anodes (Fig. 18). This can be explained by the beam fiducial volume geometry which is well defined in the vertical direction ($\pm 90$ mm) but with horizontal limits fixed only as a compromise between striving to enhance statistics and to minimize the background of electrons originating from the MWPC frames.

In the case of V-track events, in addition to the background discussed above, events for which the backscattering took place in the surrounding of the Mott target induce an additional source of background. Figure 19 presents the distributions of the reconstructed $x$ component of the vertex positions for the data collected with and without Mott target. The "foil-out" distributions have been scaled appropriately by a factor deduced from the accumulated neutron beam for each setting of the Mott scatterer. The "foil-in" distributions clearly peak at the Mott target position. The broad maxima

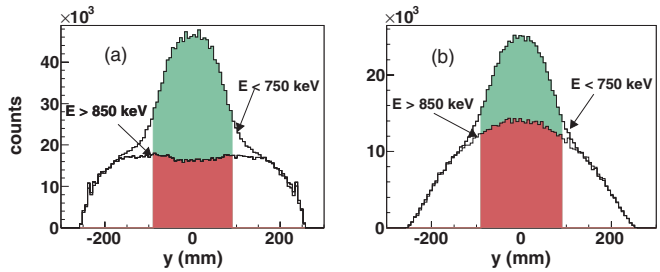


FIG. 18. (Color online) Beam profile seen in the position distribution of the extrapolated electron origins for events with a single vertex in anodes (a) and cathodes (b) for low- and high-electron energies. Shaded areas indicate the position range accepted as the "from-beam" region.

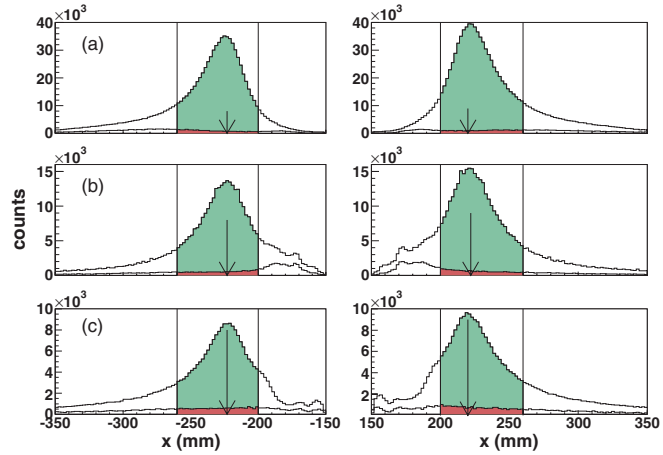


FIG. 19. (Color online) "Foil-out" background contributions (red) to the vertex $x$-coordinate position distributions of V-track events for the left and right detector side (negative and positive values of $x$ coordinate, respectively), separately for double-vertex events (a) and events with only one vertex, reconstructed in anodes (b) and cathodes (c). The arrows show the Mott foil position. Shaded areas indicate the position range accepted as "from-foil" region.

observed in "foil-out" distributions can be explained by backscattering on the MWPC material (mainly on the Ni-Cr wires and the aluminized exit window) and on the wrapping of scintillator hodoscopes. The very good signal-to-background ratio observed for the double-vertex events (≈23) decreases for single-vertex events in anodes (≈16) to reach its minimum for events with a single vertex in cathodes (≈9). The sharp structures seen in the distributions of one-vertex events, for $|x| < 200$, are due to an artifact of the reconstruction procedure caused by the assignment of single wire clusters to the discrete wire positions.

### F. $\beta$-decay asymmetry

To extract the beam polarization $P$ averaged over the beam fiducial volume the following asymmetries were analyzed:

$$\mathcal{E}(\beta,\gamma) = \frac{N^+(\beta,\gamma) - N^-(\beta,\gamma)}{N^+(\beta,\gamma) + N^-(\beta,\gamma)}, \tag{16}$$

where $N^\pm$ are experimental, background-corrected numbers of counts of single tracks, sorted in four bins of the electron velocity normalized to the speed of light $\beta = v/c$ and 11 bins of the electron emission angle $\gamma$ with respect to the neutron polarization direction. Considering only the relevant terms in Eq. (2), $N^\pm$ can be written as

$$N^\pm(\beta,\gamma) = N_0\,\epsilon^\pm[1 + \eta^\pm A\, P\overline{\beta\,\mathcal{F}(\beta,\gamma)}], \tag{17}$$

where the sign in superscripts reflects the beam polarization direction and $\beta\mathcal{F}$ is a kinematical factor corresponding to the average $z$ component of the electron velocity in a given bin of $\beta$ and $\gamma$,

$$\overline{\beta\mathcal{F}(\beta,\gamma)} = \left\langle \frac{\mathbf{v_e}}{c} \cdot \hat{\mathbf{J}} \right\rangle_{\beta,\gamma}, \tag{18}$$

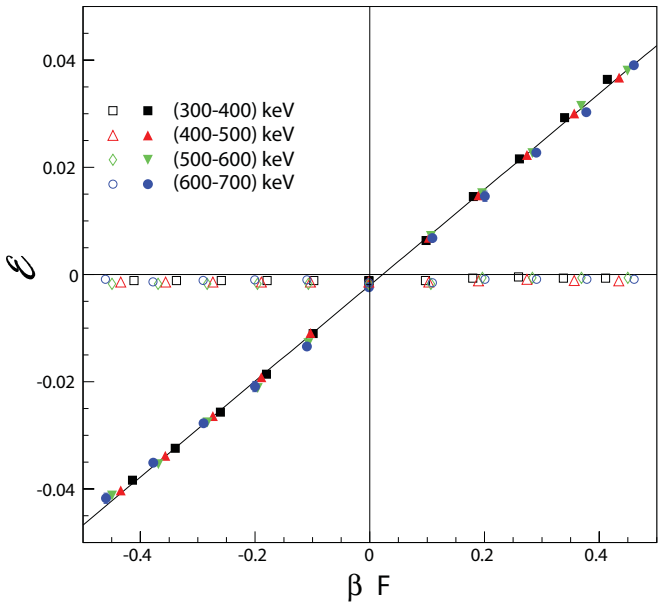


FIG. 20. (Color online) Asymmetry $\mathcal{E}$ [Eq. (19)] of signal (solid symbols) and background (open symbols) as a function of $\overline{\beta\, F}$ for different electron energy ranges for events registered on one detector side. The fit of Eq. (20) to the data allows us to extract the neutron beam polarization. A tiny negative shift of all $\mathcal{E}$ values is due to the spin-flipper influence on the detection efficiency $\epsilon^+$.

with $\hat{\mathbf{J}}$ a unit vector in the direction of the neutron polarization. The factors $\eta^{\pm}$ account for the spin-flipper efficiency. When the spin flipper is switched off one has $\eta_- \equiv 1$ (original polarization is fully maintained), whereas in the opposite case $\eta_+ = -1 + \eta$. The value $\eta \approx 0.0114$ indicates that only a very small fraction of all neutrons had not reversed their spin after passage through the spin-flipper-generated rf field. The magnitude of this effect has been investigated in a dedicated experiment [42]. The factors $\epsilon^{\pm}$ account for the influence of the spin-flipper operation on the detection efficiency of single-track events. The radiofrequency associated with the spin-flipper operation, propagating via electrical grounding and in the air via the beam line volume, increases slightly the noise level observed on the wires of MWPCs and in the hodoscopes. This increases the dead time and decreases the reconstruction efficiency. Similarly, as in the previous case, $\epsilon^- \equiv 1$ and $\epsilon^+ = 1 - \epsilon$ is close to, but less than, unity. The actual value of $\epsilon$ ($\approx$0.004) can be calculated from the total numbers of single-track events accumulated in each beam polarization state and corrected for the corresponding beam intensity. It is visible as a small negative offset of all experimental points in Fig. 20. With the above definitions, applying first-order Taylor expansion in $\epsilon$, $\eta$ and second order in the term $P\, A\, \overline{\beta\, \mathcal{F}(\beta, \gamma)}$, Eq. (16) reads,

$$\mathcal{E}\,(\beta, \gamma) = (1 - \eta/2) P\, A\, \overline{\beta\, \mathcal{F}(\beta, \gamma)} - \epsilon/2. \qquad (19)$$

Figure 20 shows the obtained $\mathcal{E}$ as a function of $\overline{\beta\, F}$ for different electron energy ranges. Taking $A$ as a constant known with very good precision ($A = -0.1173 \pm 0.0013$ [53]), the average neutron polarization can be obtained from a one-parameter fit of Eq. (19) to the experimental data.

TABLE III. Summary of neutron beam polarization analysis. Polarizations deduced from double- and single-vertex event classes ($P_{VV}$ and $P_V$) are also shown.

| Run | 100 $P$ | 100 $P_{VV}$ | 100 $P_V$ |
|---|---|---|---|
| 2003 | $80.3 \pm 1.3 \pm 1.6$ | $71.8 \pm 9.4 \pm 1.6$ | |
| 2004 | $44.2 \pm 0.4 \pm 1.5$ | $48.7 \pm 8.3 \pm 1.5$ | |
| 2006 | $80.0 \pm 1.0 \pm 1.5$ | $82.9 \pm 3.9 \pm 1.5$ | $74.1 \pm 9.5 \pm 1.5$ |
| 2007 | $77.4 \pm 0.2 \pm 0.7$ | $78.7 \pm 1.7 \pm 1.2$ | $79.9 \pm 3.0 \pm 1.2$ |

It should be noted that, in the background correction procedure, special care has been taken to ensure that the background counts do not depend on the beam polarization direction. The $\mathcal{E}$ asymmetries for events which do not originate from the beam volume (Fig. 20, open symbols), as well as of the high-energy events (above the electron end point energy), do not depend on the angle $\gamma$ and are consistent with zero polarization of their sources. Also the asymmetries for low-energy electrons (300–400 keV), for which the detection efficiency did not reach 100%, are consistent with that deduced from all other energy ranges.

The average neutron polarization values for the four data taking periods are listed in Table III. The low polarization for the 2004 data set has been traced to a bug in the guiding field found *post factum* and verified in a dedicated experiment.

The electron emission asymmetry should also be observed in Mott-scattered event classes. Due to the much lower statistics of those events, the extracted polarization $P_V$ is much less precise. However, a similar analysis has been performed and its results are in satisfactory agreement with the single-track data (Table III).

For the longest data taking period in 2007, an independent analysis of the beam polarization has been performed. This approach used the same asymmetries as defined in Eq. (16), however, with different binning. The single-track events were sorted in only 2 bins in $\gamma$ (electron emission into lower and upper hemispheres) but, additionally, in 2787 time bins (half an hour long each). This allowed us to search for a possible time dependence of the extracted polarization and daily modulations of different observables and also provided a consistency check with the previous analysis. The constant value fit to the data (Fig. 21) results in an average polarization of $0.773 \pm 0.002$, which is in very good agreement with the

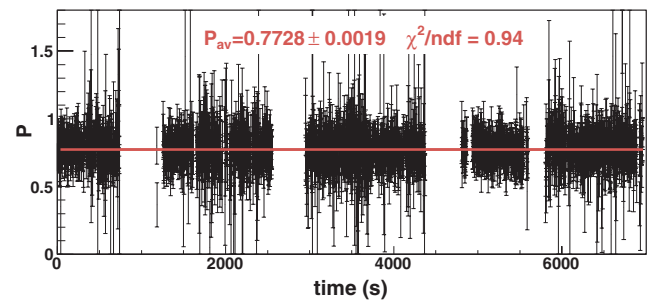


FIG. 21. (Color online) Time series of polarization extracted from the analysis of single tracks sorted in 2787 time bins. The longer breaks correspond to no-beam periods.

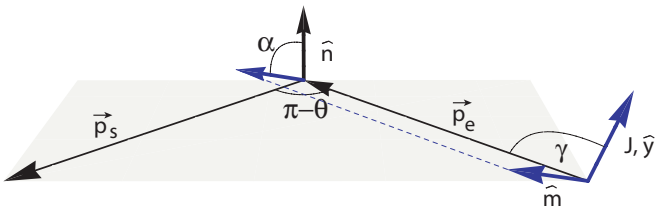


FIG. 22. (Color online) Definition of angles relevant for the analysis of the transverse electron polarization by Mott scattering. **J** is the neutron spin and $\mathbf{p_e}$, $\mathbf{p_s}$ are incident and scattered electron momenta, respectively.

result of the previous method. Considering only the statistical errors, the $\chi^2$ per degree of freedom of this fit amounts to 0.94. The discrete Fourier transform of the obtained time series is consistent with a white-noise distribution. One can conclude that no significant time dependence has been observed within about 3 months of the 2007 data collection period. For more details of this analysis and obtained limitations on some Lorenz invariance violating parameters, see Ref. [54].

### G. Correlation coefficients *R*, *N*

For the analysis of the transverse electron polarization components and the associated correlation coefficients, the method of backward Mott scattering was applied. Parity and time-reversal conservation of the spin-orbit force responsible for the spin dependence of this electromagnetic process guarantee its exclusive sensitivity to the transverse polarization component perpendicular to the scattering plane. Technically, this can be expressed by the following substitution:

$$\hat{\sigma} \rightarrow S(E,\theta)\,\hat{\mathbf{n}}, \tag{20}$$

where $S$ is the effective analyzing power of the Mott scatterer which for a given target element depends on electron energy $E$ and scattering angle $\theta$, and $\hat{\mathbf{n}}$ is a unit vector perpendicular to the Mott-scattering plane (Fig. 22),

$$\hat{\mathbf{n}} = \frac{\mathbf{p_e} \times \mathbf{p_s}}{|\mathbf{p_e} \times \mathbf{p_s}|}, \tag{21}$$

where $\mathbf{p_e}$ and $\mathbf{p_s}$ are incident and scattered electron momenta, respectively.

Applying this substitution to Eq. (2), the background-corrected experimental numbers of counts of V-track events $n^{\pm}$ can be expressed as

$$n^{\pm} = n_0\,\epsilon_v^{\pm}\{1 + \eta^{\pm} P[A\,\overline{\beta\,\mathcal{F}(\alpha)} + N\overline{S\mathcal{G}(\alpha)} + R\,\overline{\beta S\mathcal{H}(\alpha)}]\}, \tag{22}$$

where the sign in superscripts reflects the beam polarization direction; the meaning of $\epsilon_v^{\pm}$ and $\eta^{\pm}$ is the same as in the case of single-track events, Eq. (17); and the kinematic factors $\mathcal{F}(\alpha)$, $\mathcal{G}(\alpha)$, and $\mathcal{H}(\alpha)$ represent the values of the quantities $\hat{\mathbf{J}}\cdot\hat{\mathbf{p}}$, $\hat{\mathbf{J}}\cdot\hat{\boldsymbol{\sigma}}$, and $\hat{\mathbf{J}}\cdot\hat{\mathbf{p}}\times\hat{\boldsymbol{\sigma}}$, respectively (Fig. 23). The bar over a term indicates event-by-event averaging used in all analyzing methods applied in this work. In order to fully exploit the symmetry properties of both the physical problem and the experimental setup, all those quantities were sorted in 12 bins of $\alpha$, defined as the angle between the electron-scattering and

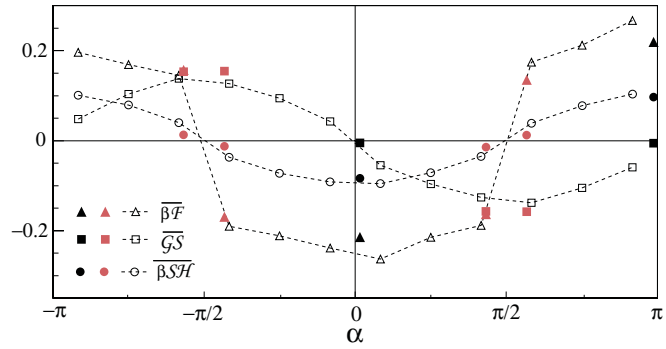


FIG. 23. (Color online) Average terms $\overline{\beta\mathcal{F}}$, $\overline{S\mathcal{G}}$, and $\overline{\beta S\mathcal{H}}$ as a function of $\alpha$ for double- (open symbols) and single-vertex events (solid black and red symbols refer to vertical and horizontal V tracks, respectively). Dotted lines are to guide the eye only. Error bars are smaller than the symbol size.

neutron-decay planes (Fig. 22), represented respectively by the $\hat{\mathbf{n}}$ and $\hat{\mathbf{m}}$ unit vectors,

$$\hat{\mathbf{m}} = \frac{\mathbf{J} \times \mathbf{p_e}}{|\mathbf{J} \times \mathbf{p_e}|}. \tag{23}$$

The $\alpha$ angle distribution of the sum $n^+ + n^-$ for all classes of the analyzed V tracks is shown in Fig. 24. The deep minima around integer multiplicities of $\pi/2$, in the distribution of double-vertex events (VV), reflect the rectangular geometry of the MWPC and are mainly shaped by limited double-track resolution of anodes and cathodes. The significantly lower intensity at negative values of $\alpha$ angle (corresponding to concave V tracks) is due to the magnetic field influence on the V-track detection efficiency, discussed in Sec. IV D.

The visible spread of the $n^+ + n^-$ distribution for "vertical" single-vertex events ($V_a$) is entirely an effect of the energy-dependent correction for the magnetic field applied to the electron trajectories. Without this correction only two discrete values (0 and $\pi$) would be possible (all relevant vectors $\mathbf{p_e}$, $\mathbf{p_s}$, and **J** are coplanar in this case).

Two different approaches have been used to obtain the $N$ and $R$ correlation coefficients. The first one, presented in the next section, can be applied to both V-track event classes, those with full geometrical information and those

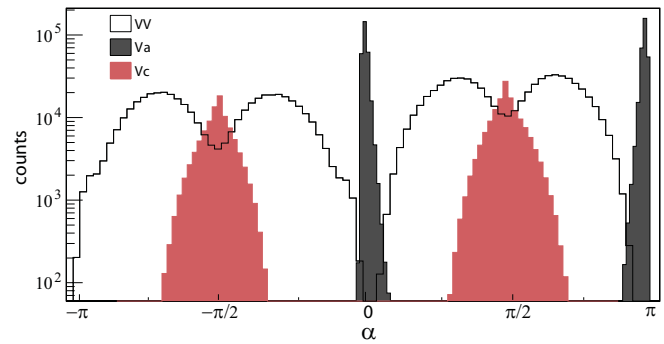


FIG. 24. (Color online) The $\alpha$ distribution ($n^+ + n^-$) of all analyzed double-vertex events ($VV$) and events with only one vertex reconstructed in anodes ($V_a$), and cathodes ($V_c$).

with only one vertex in the vertical plane. The results of this approach have been adopted as the final result of this experiment. The second approach allows the extraction of $N$ and $R$ coefficients separately from dedicated double ratios. However, in the case of the $R$ correlation this approach requires the assumption that the experimental data are symmetric with respect to the transformation $\alpha \to \alpha' = -\alpha$. This requirement is drastically violated by the influence of the spin-holding magnetic field in the case of the "vertical" V-track event class. In the case of events with full geometrical information the $\alpha \to -\alpha$ symmetry is much better fulfilled, allowing for the final application of the double-ratio method, albeit as a consistency check only.

#### 1. Correlation coefficients R, N from asymmetry

To extract the $N$ and $R$ correlation coefficients, the following set of asymmetries was considered:

$$\mathcal{A}(\alpha) = \frac{n^+(\alpha) - n^-(\alpha)}{n^+(\alpha) + n^-(\alpha)}. \tag{24}$$

Applying Eq. (22) and the first-order Taylor expansion in small quantities ($\eta$, $\epsilon_v$, $R\overline{S\beta\mathcal{H}}$, and $N\overline{S\mathcal{G}}$) and second-order Taylor expansion in the largest term, $PA\overline{\beta\mathcal{F}}$, one obtains,

$$\begin{aligned}\mathcal{A}(\alpha) = {} & P(1-\eta/2)\,[A\overline{\beta\mathcal{F}(\alpha)} + N\overline{S(\alpha)\mathcal{G}(\alpha)} \\ & + R\overline{S(\alpha)\beta\mathcal{H}(\alpha)}] - \epsilon_v/2.\end{aligned} \tag{25}$$

The term $PA\overline{\beta\mathcal{F}}$ accounts for the nonuniform illumination of the Mott foil due to the $\beta$-decay asymmetry and is known precisely from event-by-event averaging. The systematic uncertainty of this term is dominated by the error of the average beam polarization $P$. It is interesting to note that the functions $\bar{\mathcal{G}}$ and $\bar{\mathcal{H}}$ follow quite closely sine and cosine functions, respectively, and are almost orthogonal to each other. As a consequence, the covariance matrix of the two-parameter fit used to obtain the $N$ and $R$ correlation coefficients is almost diagonal, with the correlation coefficient $\rho(R, N) \approx 0.007$.

A two-parameter fit of the experimental asymmetries $\mathcal{A}$, corrected for the $PA\overline{\beta\mathcal{F}}$ term, to the experimental data set of 2007 is shown in Fig. 25. The extracted values for the $R$ and $N$ coefficients are listed in Table IV.

#### 2. Correlation coefficients R, N from double ratios

From the approximate symmetry of the detector with respect to the transformation $\alpha \to -\alpha$, it follows that $\bar{\beta}$, $\bar{S}$ and the factors $\bar{\mathcal{F}}$, $\bar{\mathcal{H}}$ are almost symmetric while $\bar{\mathcal{G}}$ is an almost antisymmetric function of $\alpha$ (Fig. 23). Applying these symmetries, the Taylor expansion as in the previous section and the definition of the quantities $n^{\pm}$, Eq. (22), one can see that the double ratio defined as

$$Q(\alpha) = \frac{(r(\alpha)-1)}{(r(\alpha)+1)}, \tag{26}$$

where

$$r(\alpha) = \sqrt{\frac{n^+(\alpha)\,n^-(-\alpha)}{n^-(\alpha)\,n^+(-\alpha)}}, \tag{27}$$

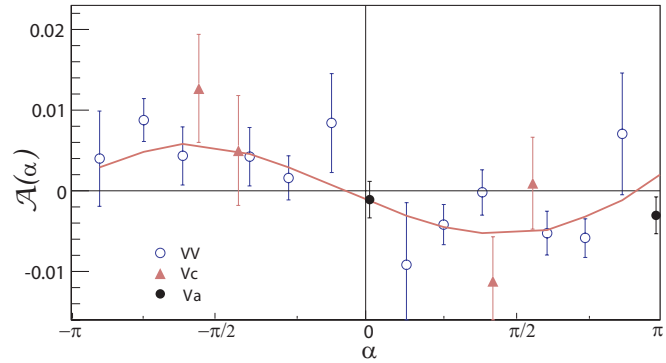


FIG. 25. (Color online) Experimental asymmetries $\mathcal{A}$ corrected for the $PA\overline{\beta\mathcal{F}}$ term as a function of $\alpha$. The solid line illustrates the two-parameter $(N, R)$ least-squares fit to the data using experimental form factors $\overline{\mathcal{SG}}$ and $\overline{\beta\mathcal{SH}}$. The indicated errors are of statistical nature.

allows us to extract the $N$ correlation coefficient according to

$$N \approx Q\frac{1 - \frac{1}{2}[(1-\eta/2)PA\overline{\beta F}]^2}{(1-\eta/2)P\overline{S\,\mathcal{G}}}. \tag{28}$$

The advantage of this method is that the effect associated with the term $PA\overline{\beta\mathcal{F}}$ is suppressed by a factor of about 60 as compared to Eq. (25). The ratio $Q$ is also insensitive to the spin-flipper-related modulation of the detection efficiency. Figure 26 shows the values of $N$ obtained as a function of the angle $\alpha$ with their average value. The good agreement between the $N$ values obtained in both ways (Table IV) enhances our confidence in the experimental values of the $N$ and $R$ coefficients obtained in the previous section.

An alternative way to extract the $R$ correlation coefficient makes use of the analysis of another ratio,

$$U(\alpha) = \frac{r'(\alpha)-1}{r'(\alpha)+1}, \tag{29}$$

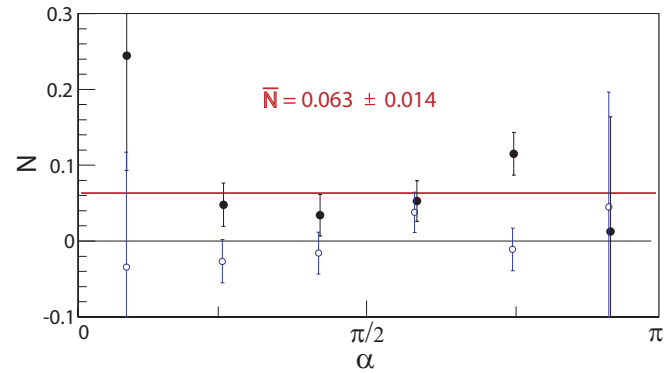


FIG. 26. (Color online) $N$ correlation coefficients calculated according to Eq. (28) for double-vertex events (solid symbols) as a function of $\alpha$ and their average. The indicated errors are of statistical nature. (Open symbols) The same but for unpolarized beam (see Sec. IV G3).

TABLE IV. Summary of results obtained in all data-collection periods. Statistical and systematic uncertainties follow the experimental values. $N_{SM}$ is the SM value of the $N$ coefficient calculated at $\bar{E}_K$. Its error comes from the experimental uncertainty of the decay asymmetry parameter $A$ [53]. The difference, as compared to the results presented in Ref. [31], is due to an improved determination of the effective analyzing powers and including the additional class of single-vertex events ($V$). $\chi^2$/NDF of all fits is also presented.

| Run | Ev. Class | 1000 $N_{SM}$ | 1000 $N$ [Eq. (25)] | 1000 $R$ [Eq. (25)] | $\chi^2$/NDF [Eq. (25)] | 1000 $N$ [Eq. (28)] | $\chi^2$/NDF [Eq. (28)] | 1000 $R$ [Eq. (31)] | $\chi^2$/NDF [Eq. (31)] |
|---|---|---|---|---|---|---|---|---|---|
| 2003 | VV | 71 ± 1 | 89 ± 92 ± 31 | −91 ± 137 ± 38 | 1.6 | 139 ± 124 ± 27 | 1.9 | −55 ± 152 ± 42 | 1.4 |
| 2004 | VV | 68 ± 1 | 74 ± 80 ± 17 | −136 ± 130 ± 30 | 1.8 | 171 ± 103 ± 15 | 2.0 | −59 ± 148 ± 30 | 1.5 |
| 2006 | VV | 68 ± 1 | 94 ± 35 ± 10 | −13 ± 48 ± 10 | 1.3 | 97 ± 35 ± 10 | 0.6 | −36 ± 48 ± 12 | 2.1 |
| 2006 | V | 68 ± 1 | 44 ± 109 ± 23 | −50 ± 55 ± 21 | | 53 ± 117 ± 23 | | | |
| 2007 | VV | 68 ± 1 | 59 ± 13 ± 5 | 12 ± 18 ± 6 | 1.1 | 63 ± 14 ± 5 | 1.3 | −5 ± 18 ± 6 | 0.7 |
| 2007 | V | 68 ± 1 | 51 ± 32 ± 14 | 9 ± 20 ± 13 | | 52 ± 33 ± 5 | | | |
| Total | | | 62 ± 12 ± 4 | 4 ± 12 ± 5 | | 67 ± 11 ± 4 | | | |

where

$$r'(\alpha) = \sqrt{\frac{n^-(\alpha)\,n^-(-\alpha)}{n^+(\alpha)\,n^+(-\alpha)}}. \tag{30}$$

Applying Eq. (22) and keeping only terms linear in small quantities ($\epsilon_v$, $PA\overline{\beta F}$, $PR\overline{\beta S\mathcal{G}}$), one can show that

$$R \approx \frac{U - (1-\eta/2)PA\overline{\beta F} - \epsilon_v/2}{(1-\eta/2)P\overline{\beta S\mathcal{H}}}. \tag{31}$$

In this method one suppresses the term proportional to the $N$ correlation. It is, however, sensitive to the "false" asymmetry due to the term $PA\overline{\beta\mathcal{F}}$ and to the spin-flipper-related modulation of the detection efficiency and, therefore, has no clear advantage over the method based on Eq. (25). Moreover, since the distribution of events with only one vertex in anodes is not symmetric with respect to the transformation $\alpha \to -\alpha$ (Fig. 24), this approach can not be applied to this event class. Figure 27 shows the obtained values of $R$ as a function of the angle $\alpha$ with their average. The results for the double-vertex event class are shown in Fig. 27 as a function of $\alpha$ with their average and are also included in Table IV.

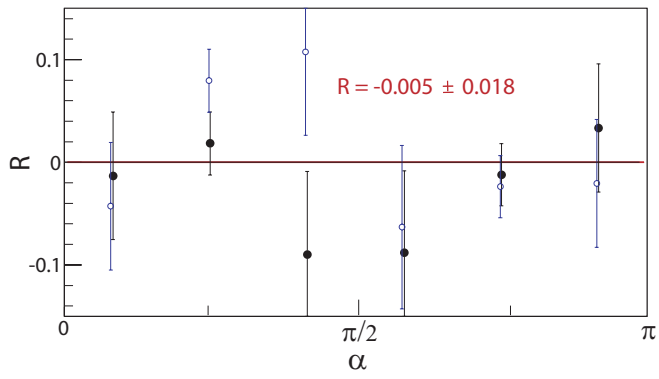


FIG. 27. (Color online) $R$ correlation coefficient calculated according to Eq. (31) for each $\alpha$ bin for double-vertex events. Only statistical errors are indicated.

### 3. *Polarization of background and unpolarized beam*

An important consistency check of the analysis of the Mott-scattered events relied on the determination of the background polarization. As there was no conceivable mechanism which could cause such polarization the expected value was zero. To check this presumption, the asymmetries as defined in Eqs. (16) and (24) have been calculated for events with energy larger than the neutron $\beta$-decay end-point energy (Figs. 28 and 30) and for events originating outside the beam fiducial volume (Fig. 20). It turned out that within the statistical accuracy all asymmetries were consistent with zero. This proves that the analysis was not biased by, for instance, a spin-flipper-related false asymmetry.

The same test has been performed for the data taken with an unpolarized beam. In this case, the analysis differed from the regular analysis of polarized beam in only one detail: Each two consecutive spin states corresponding to one flipper "on" and one flipper "off" periods were concatenated into a new one called "spin-up," while the next two were used to obtain a new "spin-down" state. This construction assures averaging of the polarization over an equal number of neutrons in both spin states and, hence, leads to an unpolarized beam (we neglect here the effect due to spin-flipper inefficiency, which is well below the statistical accuracy of this analysis).

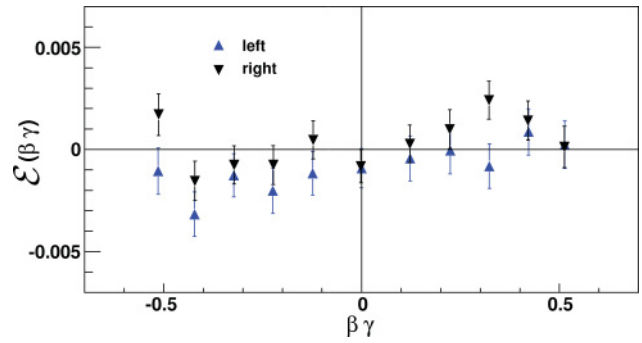


FIG. 28. (Color online) Asymmetry $\mathcal{E}(\beta,\gamma)$ for single-track events with energy larger than the neutron $\beta$-decay end-point energy, separately for the left and right detector sides. The constant value fit to the data points yields −0.00092(34) and 0.00027(28) with $\chi^2$/NDF 9.9/10 and 17.1/10 for the left and right detector sides, respectively.

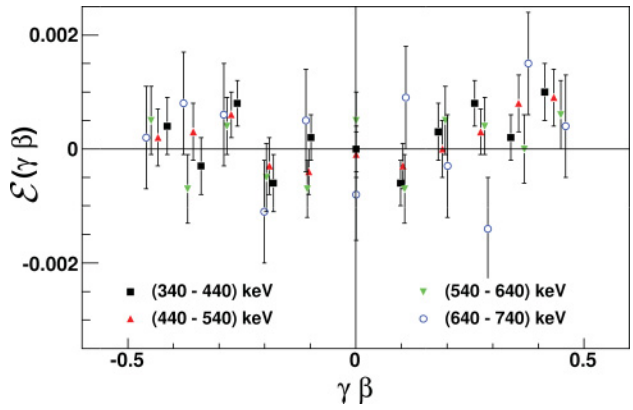


FIG. 29. (Color online) Asymmetry $\mathcal{E}(\beta,\gamma)$ for single-track events and an unpolarized beam. Both detector sides have been added together. The constant value fit to all data points yields 0.00013(7) with $\chi^2$/NDF 44.7/43.

Moreover, in this case, the asymmetries were consistent with zero (Fig. 29) what strengthens the confidence in the obtained final results.

### H. Systematic errors

The systematic uncertainties involved in the evaluation of the $R$ and $N$ coefficients are dominated by effects introduced by the background subtraction procedure and the choice of specific values of the cuts which determine whether an individual event is attributed to the "signal" or to the "background."

A "signal" event is defined as an electron originating from the free neutron decay and backscattered off the Mott target. From this definition it follows that the set of necessary conditions describing such events must include: (i) geometrical limitations to the beam volume, (ii) specification of the allowed energy range, and (iii) geometrical limitation to the area of the Mott target applied to the reconstructed scattering vertex. As a general rule, the symmetry of the detector setup has been preserved in the definition of cuts. The single exception

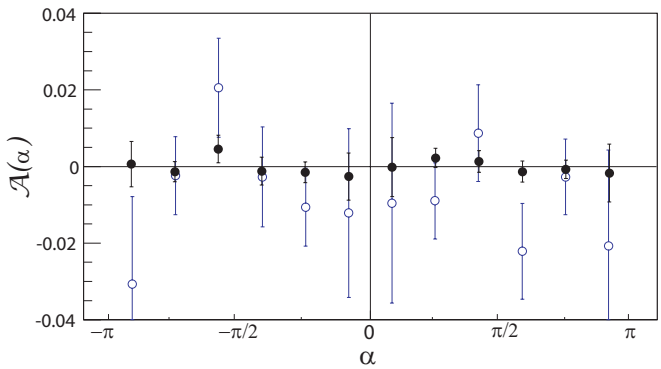


FIG. 30. (Color online) Asymmetry $\mathcal{A}(\alpha)$ for double-vertex events with energy larger than the neutron $\beta$-decay end-point energy (open symbols) and for the unpolarized beam (solid symbols). The constant value fit to the data points yields 0.0050(37) and 0.0002(9) with $\chi^2$/NDF 9.4/11 and 4.9/11 for open and solid symbols, respectively.

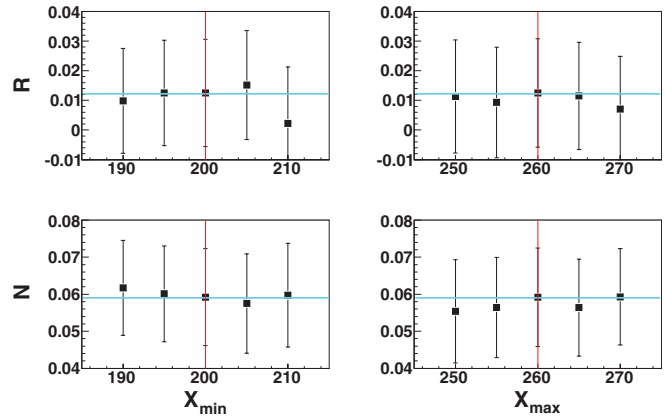


FIG. 31. (Color online) Influence of the geometrical definition of the accepted scattering vertex positions on the reconstructed $R$ and $N$ correlation coefficients. Vertical lines indicate values applied in the analysis.

from this rule was made for the beam limitation along the $y$ coordinate: the cutting line was inclined by an angle of about 1° in accordance with the beam divergence. This allowed limiting the number of parameters to the following three groups (see also Fig. 3):

(i) "from-/off-beam" definition: $y_{1_{\max}}$, $z_{1_{\max}}$, $y_{2_{\max}}$,
(ii) from/off neutron decay: $E_{L_{\min}}$, $E_{L_{\max}}$, $E_{H_{\min}}$, $E_{H_{\max}}$,
(iii) from Mott foil: $X_{\min}$, $X_{\max}$, $W_{\max}$ (side length of the square indicating the foil area in the $y$-$z$ plane).

Those parameters were used to classify an event as belonging to the following:

(i) signal:

$$\begin{aligned} |y| &< y_{1_{\max}}, \quad |z| < z_{1_{\max}}, \\ E &> E_{L_{\min}}, \quad E < E_{L_{\max}}, \\ X_{\min} > X > X_{\max}, &\quad |Y| < W_{\max}, \quad |Z| < W_{\max}, \end{aligned} \tag{32}$$

(ii) off-beam background: as above but

$$|y| > y_{2_{\max}}, \tag{33}$$

(iii) high-energy background:

$$\begin{aligned} |y| &< y_{1_{\max}}, \quad |z| < z_{1_{\max}}, \\ E &> E_{H_{\min}}, \quad E < E_{H_{\max}}, \\ X_{\min} > X > X_{\max}, &\quad |Y| < W_{\max}, \quad |Z| < W_{\max}, \end{aligned} \tag{34}$$

where $(x=0, y, z)$ and $(X, Y, Z)$ denote coordinates of the electron origin and the Mott-scattering vertex, respectively. Due to the limited accuracy of the reconstructed energies and trajectories, for each of those parameters there exists a certain range of values which seems to be almost equivalent. In the analysis, however, the specific values can generate slightly different final results. In order to estimate this effect, the corresponding ranges of acceptance have been identified individually for each parameter and the final analysis was repeated varying one parameter in its range with all others fixed in the center of their ranges. The maximal deviations of the resulting $R$ and $N$ coefficients from the central values were taken as maximal errors. Figure 31 presents the result of such

TABLE V. Summary of systematic errors for the 2007 data set. The ranges over which individual parameters have been varied in the error estimation procedure are shown.

| Source | 10 000 $\delta N$ | 10 000 $\delta R$ |
|---|---|---|
| $y_{1_{\max}} \in (80, 95)$ | 20 | 17 |
| $z_{1_{\max}} \in (240, 250)$ | 16 | 9 |
| $y_{2_{\max}} \in (100, 120)$ | 26 | 25 |
| $E_{L_{\min}} \in (200, 260)$ | 13 | 11 |
| $E_{L_{\max}} \in (580, 660)$ | 18 | 15 |
| $E_{H_{\min}} \in (780, 860)$ | 5 | 4 |
| $E_{H_{\max}} \in (1400, 1900)$ | 7 | 16 |
| $X_{\min} \in (190, 210)$ | 11 | 18 |
| $X_{\max} \in (245, 265)$ | 15 | 18 |
| $W_{\max} \in (210, 230)$ | 19 | 23 |
| Term $PA\overline{\beta\mathcal{F}}$ | 6 | 30 |
| Effective Sherman function $\bar{S}$ | 13 | 4 |
| Guiding field misalignment | 3 | 7 |
| Dead time variations | 9 | 0.5 |
| Total | 54 | 61 |

analysis for parameters limiting the geometrical position of the Mott-scattering vertices. The contributions of all parameters to the final uncertainty, as well as their ranges used in this analysis, are collected in Table V.

It should be noted that the vertical alignment of the apparatus with respect to the neutron beam has been verified to a precision below 1 mm using the reconstructed centroid of the beam profile (Figs. 17 and 18). A similar precision of alignment with respect to the magnet setup and the beam axis was maintained for all other detector components except the Mott-scattering target. Here the accuracy of positioning in the $x$ coordinate was about $\pm 2$ mm. This is still acceptable considering the vertex reconstruction accuracy of the MWPCs (Fig. 19).

The next important systematic uncertainty is due to the limited accuracy of the determination of the average beam polarization. All measured asymmetries used for the evaluation of individual correlation coefficients are proportional to the product of this coefficient and the beam polarization. As a consequence, the relative error of the extracted coefficient must be larger than that of the polarization.

The situation is even more difficult for the $R$ correlation. With a vertically polarized neutron beam the existence of a nonzero value of this correlation would result in a difference between the number of electrons backscattered into the upper and into the lower hemisphere. The same effect is generated by the $\beta$-decay asymmetry ($A$ correlation), appearing as a term $PA\overline{\beta\mathcal{F}}$ in Eqs. (25) and (31). What makes the link between the $A$ and $R$ correlations so special is the shape of the corresponding average form factors $\bar{\mathcal{F}}$ and $\bar{\mathcal{H}}$ (Fig. 23). They both exhibit the same symmetry properties with respect to $\alpha$, so the effects generated by each of them are almost indistinguishable.

The cleanest, but also most unpractical, way to avoid this interference would be to confine the electron emission angle to 90°, in which case $\bar{\mathcal{F}} \equiv 0$. With a finite accepted solid angle, one is forced to apply a suitable correction in the form of the

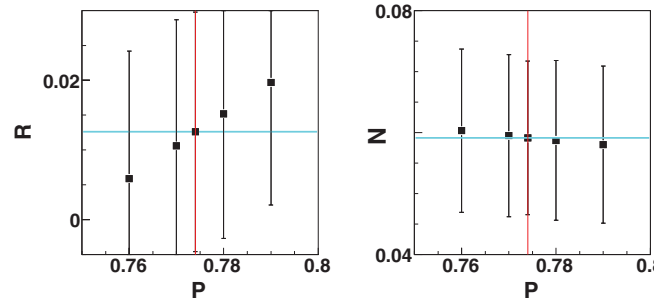


FIG. 32. (Color online) Dependence of the reconstructed $R$ and $N$ correlation coefficients on the value of the neutron beam polarization. Vertical lines indicate values applied in the analysis. The strong correlation between $R$ and $P$ is due to the $P\beta A\bar{\mathcal{F}}$ term in Eq. (25).

$PA\overline{\beta\mathcal{F}}$ term. Since the electron momenta after emission and after scattering are reconstructed, the necessary form-factors ($\bar{\mathcal{F}}$, $\bar{\mathcal{G}}$, $\bar{\mathcal{H}}$) are known to a high precision for the entire event sample, and the main impact of the applied correction is due to the uncertainty of the neutron polarization. To evaluate the magnitude of the influence of this term on the final result, the fit with $R$ and $N$ as free parameters was repeated with $P$ varied by one standard deviation of the total neutron polarization uncertainty (Fig. 32). The obtained difference enters the budget of the systematic errors and is presented in Table V.

Despite the careful design and manufacturing of the large-volume electromagnet responsible for the spin-holding magnetic field, the mapping of this field at the experimental position showed a small misalignment with respect to the vertical direction and nonuniformities in the beam fiducial volume. The average effect was accounted for in the analysis by appropriate rotation of the neutron polarization direction. A residual systematic effect (Table V) was induced by the uncertainty of the field measurements and by the observed stability of the ambient magnetic field at the experimental position. Since the radiofrequency signal of the spin flipper was a source of small noise in the readout electronics, tiny dead-time variations correlated with the spin flipper were observed. Their influence on the result was corrected for. The residual effect is included in Table V.

In the final error analysis it has been assumed that the sources contributed independently, and so these were added quadratically to obtain the final systematic uncertainty.

## V. RESULTS

Combining the results from all runs leads to the following final result (Table IV):

$$R = 0.004 \pm 0.012_{\text{stat}} \pm 0.005_{\text{syst}}, \tag{35}$$

$$N = 0.067 \pm 0.011_{\text{stat}} \pm 0.004_{\text{syst}}. \tag{36}$$

In Figs. 33 and 34 the new results are presented as exclusion plots containing in addition the experimental information available to date from nuclear and neutron $\beta$ decays, as surveyed in Ref. [24]. The upper part of Fig. 33 contains plots corresponding to the real and imaginary parts of the normalized

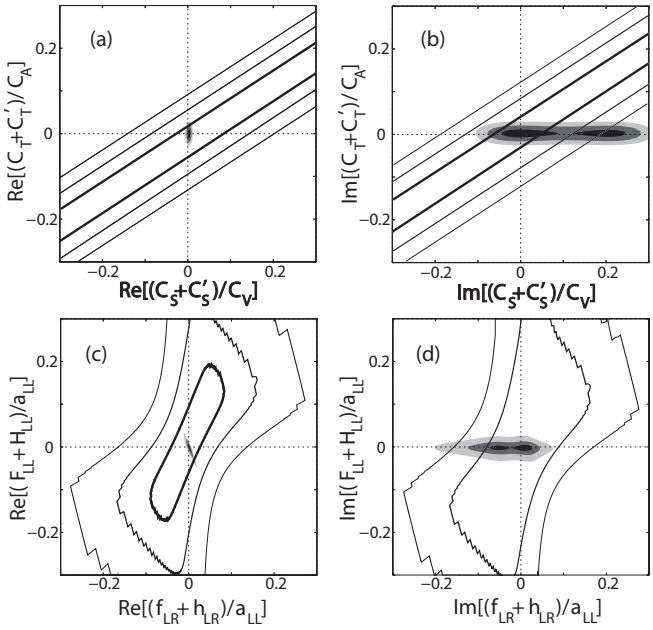


FIG. 33. Experimental bounds on the scalar vs. tensor normalized couplings [(a) and (b)] and leptoquark exchange helicity projection amplitudes [(c) and (d)]. The gray areas represent the information as defined in Ref. [24], while the lines represent the limits resulting from the present experiment. Decreasing line thickness as well as intensity of the gray areas correspond to 1-, 2- and 3-$\sigma$ confidence levels.

scalar and tensor coupling constants $S$ and $T$, Eqs. (9) and (10). The present accuracy of the determination of the $N$ correlation coefficient does not improve the already strong constraints on the real part of the couplings (left panel). It is, however, consistent with the existing data and, in addition, adds confidence to the validity of the extraction of the $R$ correlation coefficient. The latter constrains significantly the imaginary part of the scalar couplings, beyond the limits from all previous measurements (right panel). Moreover, in this case, the result is consistent with the SM ($C_S = C'_S = C_T = C'_T = 0$) and with time-reversal invariance.

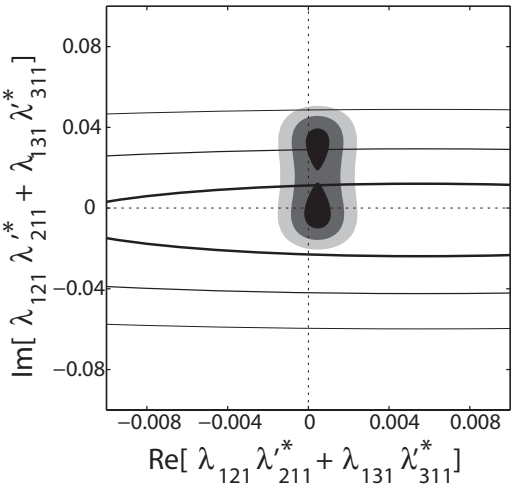


FIG. 34. Experimental bounds on the real vs. imaginary combined couplings of MSSM with $R$-parity violation. The gray areas represent the information as defined in Ref. [24], while the lines represent the limits resulting from the present experiment. Decreasing line thickness and intensity of the gray areas correspond to 1-, 2- and 3-$\sigma$ confidence levels.

In the lower part of Fig. 33 the same convention was used to illustrate the constraints (existing and resulting from the present work) to the helicity projection amplitudes in the leptoquark exchange model, as defined in Ref. [2]. In this formalism $F_{LL}$, $f_{LR}$ and $H_{LL}$, $h_{LR}$ correspond to leptoquarks with charge $|Q| = 2/3$ and $|Q| = 1/3$, respectively. Capital letters correspond to the scalar (spin-zero) while lowercase letters describe vector (spin-one) leptoquarks exchange amplitudes. Subscripts indicate the helicity structure of the underlying interaction. As in the previous case, only the $R$ correlation reveals evident exclusion power and allows a significant improvement of the constraints on the imaginary part of the vector leptoquark amplitudes ($f_{LR} + h_{LR}$).

Similar constraints can be imposed on the selectron exchange couplings ($\lambda_{1i1}$, $\lambda_{i11}$) in the minimal supersymmetric standard model (MSSM) with $R$-parity violation. Adopting conventions used in Ref. [55], the amplitude of the selectron ($\tilde{e}$) exchange between the quark and lepton can be written as

$$y\mathcal{M}_{\tilde{e}_L} = \sum_{i=2,3} \frac{\lambda_{1i1}\lambda'^{*}_{i11}}{4m^2_{\tilde{e}_{Li}}}\,\bar{u}(1+\gamma_5)d\bar{e}(1-\gamma_5)\nu_e, \qquad (37)$$

where $m_{\tilde{e}_L}$ is the slepton mass assumed to be equal to 100 GeV. According to Ref. [55], the contribution of the selectron exchange to the scalar coupling of the $\beta$ decay and to the $R$ and $N$ correlations can be written as

$$C_S = g_s \sum_{i=2,3} \frac{\lambda_{1i1}\lambda'^{*}_{i11}}{4m^2_{\tilde{e}_{Li}}}, \qquad (38)$$

$$R = -\lambda \frac{2\sqrt{2}\,\mathrm{Im}C_S}{G_F\,V_{u,d}\,g_V(1+3\lambda^2)}, \qquad (39)$$

$$N = -\lambda \frac{2\sqrt{2}\,\mathrm{Re}C_S}{G_F\,V_{u,d}\,g_V(1+3\lambda^2)}, \qquad (40)$$

where $g_s$ is given by the neutron, proton, and light quarks masses,

$$g_s = \frac{M_n - M_p}{m_u - m_d} \approx 0.49 \pm 0.17, \qquad (41)$$

where $V_{ud} = 0.97425(22)$ is the CKM matrix element, $\lambda = -1.2694(28)$, and $G_F = 1.166364(5) \times 10^{-5}$ GeV$^{-2}$ [53].

The presently best direct constraint for the imaginary part of the scalar interaction obtained in the present experiment improves significantly the limits on the combination of coupling constants leading to the updated version of the exclusion plot presented in Ref. [55] (Fig. 34).

The real part of this combination was also accessible in this experiment via the measurement of the $N$ correlation. The achieved accuracy, even if slightly better than that for $R$, cannot compete with the much more precise data adopted from the compilation of superallowed Fermi nuclear $\beta$ decays.

## VI. CONCLUSION

The measurement of the transverse polarization components of electrons from the decay of free polarized neutrons has been carried out successfully. This was the first experimental determination of the $R$ correlation coefficient in neutron $\beta$ decay and, to our knowledge, also the first observation of the finite value of the $N$ correlation, an effect of the final-state interaction in the neutron $\beta$ decay. The obtained results allowed a significant improvement in constraining the relative strength of exotic, scalar-type weak interaction and related parameters in standard-model extensions with leptoquark exchange and in the MSSM with $R$-parity violation beyond the limits from all previous measurements.

The most important feature of the experimental setup which made this possible was the ability to fully reconstruct momenta of low-energy electrons before and after the backward Mott scattering which served as the electron polarization analyzer. Further, even substantial improvement in the statistical accuracy of the determination of $R$ and $N$ correlation coefficients can be achieved in an experiment based on this principle, provided that a substantial increase of the solid angle acceptance is attained.

## ACKNOWLEDGMENTS

Special thanks are due to ETH Zurich for the continuous support and to Jerzy Sromicki for his leading role at the initial phase of this project. This work was supported in part by the Polish Committee for Scientific Research under Grants No. 2P03B11122 and No. N202 047037, by an Integrated Action Program Polonium (Contract No. 05843UJ), and by the FWO Vlaanderen. Part of the computational work was performed at ACK Cyfronet, Kraków. The collaboration is grateful to PSI for excellent support and kind hospitality.

[1] H. Abele, Prog. Part. Nucl. Phys. **60**, 1 (2008).
[2] P. Herczeg, Prog. Part. Nucl. Phys. **46**, 413 (2001).
[3] J. Erler and M. Ramsey-Musolf, Prog. Part. Nucl. Phys. **54**, 351 (2005).
[4] M. Kobayashi and T. Maskawa, Prog. Theor. Phys. **49**, 652 (1973).
[5] J. H. Christenson *et al.*, Phys. Rev. Lett. **13**, 138 (1964).
[6] K. Abe *et al.*, Phys. Rev. D **66**, 071102 (2002).
[7] B. Aubert *et al.*, Phys. Rev. Lett. **89**, 011802 (2002).
[8] A. D. Sakharov, JETP Lett. **5**, 24 (1967).
[9] M. Trodden, Rev. Mod. Phys. **71**, 1463 (1999).
[10] L. K. Gibbons *et al.*, Phys. Rev. Lett. **70**, 1199 (1993).
[11] J. M. Drake, E. G. Bilpuch, G. E. Mitchell, and J. F. Shriner, Phys. Rev. C **49**, 411 (1994).
[12] C. Baker *et al.*, Phys. Rev. Lett. **97**, 131801 (2006).
[13] J. Hudson *et al.*, Nature **473**, 493 (2011).
[14] W. C. Griffith, M. D. Swallows, T. H. Loftus, M. V. Romalis, B. R. Heckel, and E. N. Fortson, Phys. Rev. Lett. **102**, 101601 (2009).
[15] A. Czarnecki and B. Krause, Phys. Rev. Lett. **78**, 4339 (1997).
[16] S. Dar, arXiv:hep-ph/0008248v2 (2002).
[17] A. Angelopoulos *et al.*, Phys. Lett. B **444**, 43 (1998).
[18] A. Alavi-Harati *et al.*, Phys. Rev. Lett. **84**, 408 (2000).
[19] V. Abazow *et al.* (Do Collaboration), Phys. Rev. D **82**, 032001 (2010).
[20] J. D. Jackson *et al.*, Nucl. Phys. **4**, 206 (1957).
[21] R. B. Curtis and R. R. Lewis, Phys. Rev. **107**, 543 (1957).
[22] M. Abe *et al.*, Phys. Rev. Lett. **93**, 131601 (2004).
[23] T. Yamazaki *et al.*, Phys. Rev. Lett. **104**, 083401 (2010).
[24] N. Severijns, M. Beck, and O. Naviliat-Cuncic, Rev. Mod. Phys. Sect. A **78**, 991 (2006).
[25] R. Huber *et al.*, Phys. Rev. Lett. **90**, 202301 (2003).
[26] P. Vogel and B. Werner, Nucl. Phys. **404**, 345 (1983).
[27] M. Clark, J. Robson, and R. Nathans, Phys. Rev. Lett. **1**, 100 (1958).
[28] L. Lising *et al.*, Phys. Rev. C **62**, 055501 (2000).
[29] T. Soldner *et al.*, Phys. Lett. B **581**, 49 (2004).
[30] H. Mumm *et al.*, arXiv:1104.2778v2 (2011).
[31] A. Kozela *et al.*, Phys. Rev. Lett. **102**, 172301 (2009).
[32] T. Lee and C. Yang, Phys. Rev. **104**, 254 (1956).
[33] N. Danneberg *et al.*, Phys. Rev. Lett. **94**, 021802 (2005).
[34] M. B. Schneider, F. P. Calaprice, A. L. Hallin, D. W. MacArthur, and D. F. Schreiber, Phys. Rev. Lett. **51**, 1239 (1983).
[35] G. Ban *et al.*, Nucl. Instrum. Methods A **565**, 711 (2006).
[36] R. Kossakowski *et al.*, Nucl. Phys. A **503**, 473 (1989).
[37] P. Liaud *et al.*, Nucl. Phys. A **612**, 53 (1997).
[38] A. Schebetov *et al.*, Nucl. Instrum. Methods B **94**, 575 (1994).
[39] P. Boni, Physica B **234–236**, 1038 (1997).
[40] A. Schebetov *et al.*, J. Phys. Soc. Jpn. **65**, 195 (1996).
[41] A. Schebetov *et al.*, Nucl. Instrum. Methods A **432**, 214 (1999).
[42] J. Zejma *et al.*, Nucl. Instrum. Methods A **539**, 622 (2004).
[43] N. Sherman, Phys. Rev. **103**, 1601 (1956).
[44] S. Agostinelli *et al.*, Nucl. Instrum. Methods A **506**, 250 (2003).
[45] F. Salvat *et al.*, Comput. Phys. Commun. **165**, 157 (2005).
[46] M. A. Khakoo, D. Roundy, C. Hicks, N. Margolis, E. Yeung, A. W. Ross, and T. J. Gay, Phys. Rev. A **64**, 052713 (2001).
[47] A. Gellrich and J. Kessler, Phys. Rev. A **43**, 204 (1991).
[48] J. Sromicki *et al.*, Phys. Rev. Lett. **82**, 57 (1999).
[49] A. Kozela, A. Białek, K. Bodek, P. Gorel, S. Kistryn, E. Stephan, and J. Zejma, Nucl. Instrum. Methods B **269**, 1767 (2010).
[50] C. Hilbes, Ph.D. thesis, ETH, Zürich 2001.
[51] S. Kistryn, *Readout System for Medium-Size Experiments, Advanced Knowledge Application in Practice*, edited by I. Fuerstner (SCIYO in Rijeka, 2010), p. 243.
[52] N. Kurz and H. Essel, *GSI Multi-Branch System User Manual* (GSI, Darmstadt, 1999).
[53] K. Nakamura *et al.* (Particle Data Group), J. Phys. G **37**, 075021 (2010).
[54] A. Kozela *et al.*, *Proceedings of the Fifth Meeting on CPT and Lorentz Symmetry*, edited by A. Kostelecky (World Scientific Publishing Company, Singapore, 2010), p. 174.
[55] N. Yamanaka, T. Sato, and T. Kubota, J. Phys. G **37**, 055104 (2010).